

When Does Global Attention Help? A Unified Empirical Study on Atomistic Graph Learning

Arindam Chowdhury and Massimiliano Lupo Pasini

Computational Sciences and Engineering Division (CSED), Oak Ridge National Laboratory, 5700, 1 Bethel Valley Rd, Oak Ridge, 37830, TN, USA.

*Corresponding author(s). E-mail(s): lupopasinim@ornl.gov;
Contributing authors: chowdhurya1@ornl.gov;

Abstract

Graph neural networks (GNNs) are widely used as surrogates for costly experiments and first-principles simulations to study the behavior of compounds at atomistic scale, and their architectural complexity is constantly increasing to enable the modeling of complex physics. While most recent GNNs combine more traditional message passing neural networks (MPNNs) layers to model short-range interactions with more advanced graph transformers (GTs) with global attention mechanisms to model long-range interactions, it is still unclear when global attention mechanisms provide real benefits over well-tuned MPNN layers due to inconsistent implementations, features, or hyperparameter tuning. We introduce the first unified, reproducible benchmarking framework—built on HydraGNN—that enables seamless switching among four controlled model classes: MPNN, MPNN with chemistry/topology encoders, GPS-style hybrids of MPNN with global attention, and fully fused local–global models with encoders. Using seven diverse open-source datasets for benchmarking across regression and classification tasks, we systematically isolate the contributions of message passing, global attention, and encoder-based feature augmentation. Our study shows that encoder-augmented MPNNs form a robust baseline, while fused local–global models yield the clearest benefits for properties governed by long-range interaction effects. We further quantify the accuracy–compute trade-offs of attention, reporting its overhead in memory. Together, these results establish the first controlled evaluation of global attention in atomistic graph learning and provide a reproducible testbed for future model development.

Keywords: Message Passing Neural Network, Equivariant Graph Neural Networks, Long-range Interactions, Graph Transformer, Topological and Chemical Encoders

This manuscript has been authored in part by UT-Battelle, LLC, under contract DE-AC05-00OR22725 with the US Department of Energy (DOE). The US government retains and the publisher, by accepting the article for publication, acknowledges that the US government retains a nonexclusive, paid-up, irrevocable, worldwide license to publish or reproduce the published form of this manuscript, or allow others to do so, for US government purposes. DOE will provide public access to these results of federally sponsored research in accordance with the DOE Public Access Plan (<http://energy.gov/downloads/doe-public-access-plan>).

1 Introduction

Predicting atomistic and material properties from atomistic structure is a central challenge across computational chemistry, catalysis, and materials discovery (Butler et al. 2018; Ward et al. 2016). Traditionally, property estimation relied on (i) empirical and semi-empirical correlations—group additivity and Hammett–Taft substituent analysis, followed by QSAR/QSPR with hand-crafted descriptors (Benson 1976; Hammett 1937; Taft 1952; Cherkasov et al. 2014)—(ii) physics-based electronic-structure methods such as Hartree-Fock (HF) density functional theory (DFT), post-HF methods such as second-order Møller-Plesset (MP2) perturbation theory and coupled cluster singles, doubles, (triples) CCSD(T)) (Kohn and Sham 1965; Parr and Yang 1989; Mardirossian and Head-Gordon 2017; Bartlett and Musiał 2007; Grimme et al. 2010), (iii) molecular dynamics with empirical or *ab initio* potentials (Frenkel and Smit 2002), and (iv) direct experiments and high-throughput screening (Gregoire et al. 2013). While foundational, these approaches face limitations: QSAR and group-additivity depend on fixed descriptors with narrow domains of applicability and often miss nonlocal, conformational, or environment effects; DFT/post-HF deliver systematic accuracy but scale steeply (roughly $\mathcal{O}(N^{3-4})$ for Kohn–Sham DFT and $\mathcal{O}(N^7)$ for CCSD(T)) and can struggle with dispersion or strong correlation without specialized corrections (Mardirossian and Head-Gordon 2017; Grimme et al. 2010; Bartlett and Musiał 2007); MD accuracy hinges on force-field fidelity and long trajectories to sample rare events (Frenkel and Smit 2002); and experiments are costly, lower-throughput, and condition-specific (Gregoire et al. 2013). In contrast, modern machine learning (ML)-based methods amortize expensive computation/measurement into training and then yields fast, scalable inference while capturing complex, nonlocal structure–property relationships from 2D/3D atomistic representations (Behler and Parrinello 2007; Rupp et al. 2012; Smith et al. 2017; Butler et al. 2018; Ward et al. 2016).

Graph-based learning offers a natural paradigm: a molecule can be modeled as a graph whose nodes (atoms) and edges (bonds or distance-thresholded connections) carry domain-specific attributes, optionally augmented with 3D coordinates in geometric graphs (Duvenaud et al. 2015; Kearnes et al. 2016; Gilmer et al. 2017; Schütt et al. 2018b; Klicpera et al. 2020b). Such a structure supports inductive biases – permutation invariance and, when needed, euclidean equivariance – that are essential for modeling scalar, vector, and tensor targets (Zaheer et al. 2017; Bronstein et al. 2021; Thomas et al. 2018; Fuchs et al. 2020; Garcia Satorras et al. 2021). Graph Neural Networks (GNN) (Battaglia et al. 2018; Zhou et al. 2020; Wu et al. 2021) including both message-passing neural networks (MPNN) (Gilmer et al. 2017) and their geometric extensions (e.g., SchNet, DimeNet, EGNN) (Schütt et al. 2018b; Klicpera et al.

2020d; Garcia Satorras et al. 2021) can then leverage the connectivity structure for predicting atomistic properties.

Despite their success, MPNNs can struggle when target properties depend on *long-range interactions* (LRI)—such as electrostatics, induction, and dispersion—that persist beyond small k -hop neighborhoods or bond-local connectivity (London 1937a; Casimir and Polder 1948b; Israelachvili 2011; Stone 2013). Particularly, nonlocal effects due to LRI arise when influential atoms are far in either sense and recaps their physical scalings (e.g., $-C_6/R^6$ dispersion) (London 1937a; Stone 2013). Deepening MPNNs to enlarge the receptive field invites two well-known pathologies, *over-smoothing* and *over-squashing* (Li et al. 2018a; Oono and Suzuki 2020a; Alon and Yahav 2021a; Toppling et al. 2022). These limitations argue for mechanisms that propagate information globally without sacrificing local structural details. Transformer-style global attention provides such a mechanism (Vaswani et al. 2017). Graph Transformers (GTs) replace fixed-radius aggregation with learnable all-to-all information flow via multi-head self-attention, potentially capturing both local and global dependencies in a single layer (Dwivedi and Bresson 2020; Kreuzer et al. 2021; Ying et al. 2021c). However, naively applying dense attention over N nodes incurs $\mathcal{O}(N^2)$ time and memory per layer, which can be prohibitive for large atomistic graphs (Vaswani et al. 2017). Hybrid designs (e.g., GPS (Rampásek et al. 2022) have been proposed to combine the modeling capabilities of strong local message passing with global attention mechanisms that sparsify the connectivity of the graph to contain their computational cost. However, these methods have only been evaluated on a small group of datasets and over a limited class of MPNNs as local information aggregators.

In this work, we present a unified, reproducible framework built on top of HydraGNN (Lupo-Pasini et al. 2022b) – a highly parallelized graph multi-task learning pipeline – for systematically evaluating transformer-based graph models for atomistic property prediction alongside a large class of SOTA MPNNs, including equivariant MPNNs. The framework instantiates four controlled configurations: (i) MPNN, (ii) MPNN with chemistry-/topology-based encoders, (iii) GPS-style MPNN with global attention, and (iv) a fused local–global model with domain-specific encoders. The compact encoder suite supplies chemically and structurally informative inputs: per-atom physico-chemical descriptors, node/edge structural features (e.g., degree, centralities, clustering, k -core, edge indices), and Laplacian positional encodings; edges additionally carry bond and, when available, distance information. Lightweight linear embeddings integrate these channels, and training uses distributed data parallelism (DDP) with automated hyperparameter optimization to enable fair ablations. Across twelve benchmarks spanning regression and classification, we assess (1) when global attention yields gains beyond well-tuned MPNNs, (2) the contribution of domain/topological encoders, and (3) the accuracy–compute trade-off associated with the quadratic cost of attention. Empirically, encoders systematically improve performance while attention alone is not uniformly superior. Fused local–global models provide the largest benefits on tasks with significant nonlocal or geometric effects, while encoder-augmented MPNNs remain competitive on others. The result is a standardized experimental setup and sets the ground towards clarifying when opting for global attention is necessary, thereby serving as a reference point for future method development.

1.1 Related Work

GTs for molecules have seen several recent advancements. *Graphomer* injects structural biases (shortest-path, centrality, edge encodings) and achieves strong OGB results, but relies on dense quadratic attention and task-specific heuristics without controlled comparisons to equally tuned MPNNs (Ying et al. 2021b). *MAT* augments attention with RDKit features and pairwise distance biases, yet similarly inherits the quadratic cost and heavy feature engineering (Maziarka et al. 2020). Equivariant Transformers (e.g., *EquiformerV2*) improve 3D fidelity for atomistic energies/forces but are computationally demanding and targeted to continuous 3D labels rather than the broader mix of graph-level and node/edge targets considered here (Liao et al. 2024). Large-scale frameworks such as *Uni-Mol* (Zhou et al. 2023a) leverage massive SE(3)-equivariant pretraining to obtain strong downstream accuracy, but conflate architectural gains with data scale and are difficult to reproduce under typical compute budgets (Zhou et al. 2023b). Hybrid local-global designs demonstrate a general recipe that couples message passing with global attention, though evaluations emphasize non-atomistic benchmarks and do not isolate chemistry-aware encoders (Rampášek et al. 2022); follow-up work (*GPS++*) on PCQM4Mv2 shows that well-tuned message passing can retain much of the benefit with little or no attention, but focuses on a single large dataset (Masters et al. 2023a). Finally, long-range benchmarks (LRGB) motivate global receptive fields yet are not atomistic-specific and omit common chemical settings such as node-level charges or multi-label assays (Dwivedi et al. 2022). Consequently, the field lacks a controlled, reproducible study that compares these architectural choices under a common framework.

1.2 Contributions

The novelty of this work lies in providing the first controlled, reproducible framework that disentangles the effects of message passing, global attention, and encoder-based feature augmentation in atomistic graph learning. Unlike prior studies that test isolated architectures on narrow benchmarks, we systematically evaluate four model classes under a single experimental pipeline, allowing clear attribution of accuracy gains to either architecture, encoders, or their combination. To that end, we make the following key contributions:

- **Development of a unified framework to combine MPNN and GT.** We expanded the existing HydraGNN-based pipeline that provides MPNN architectures with GT architectures, and offer seamless selection of model pathways viz. MPNN-only, MPNN + Encoders, GPS-style, and fully fused (MPNN + GPS + Encoders) configurations with DDP and automated HPO (Fig. 3).
- **Inclusion of Domain/topology encoders into graph embeddings.** Chemically informed per-atom descriptors, node/edge structural encodings, and Laplacian positional encodings, integrated via lightweight embeddings (Sections 3.1-3.2).
- **Comprehensive evaluation with ablation studies.** Cross-domain study on 7 datasets (Table 1) with regression, multi-class, and multi-label tasks; quantitative comparisons (Sections 4.4.1-4.4.7).

1.3 Paper Organization

Section 2 reviews preliminaries on graphs, geometric learning, and invariance/equivariance, and motivates global attention through LRIs and MPNN limitations, then introduces GPS-style hybrids. Section 3 describes the proposed framework including encoder and embedding modules. Section 4 reports experiments, with Section 5 discussing implications and Section 6 concluding the work.

2 Background and Problem Setting

We first introduce some fundamental definitions and concepts that will be extensively used throughout this work. \mathcal{X} represents sets. $[\mathbf{X}]_{uv}$, and $[\mathbf{x}]_i$ denote the entries of a multi-dimensional matrix \mathbf{X} , and a vector \mathbf{x} . The generic subindex $:$ denotes a whole dimension, e.g., row i of matrix \mathbf{X} is denoted as $[\mathbf{X}]_{i:}$. Scalars are denoted by x or X .

2.1 Atomistic Graphs

A graph is a data structure that represents entities (nodes) and their relations (edges). Formally, $\mathcal{G} = \{\mathcal{V}, \mathcal{E}\}$ denotes an undirected graph where \mathcal{V} represents the set of nodes and \mathcal{E} represents the set of edges. $N = |\mathcal{V}|$ is the number of nodes in the graph. Each node $v \in \mathcal{V}$ supports a p -dimensional feature vector denoted by $\mathbf{x}_v \in \mathbb{R}^p$, such that $[\mathbf{X}]_{v:} = \mathbf{x}_v$, while $\mathbf{e}_{uv} \in \mathbb{R}^f$ represents edge attributes supported by each edge $(u, v) \in \mathcal{E}$ where $[\mathbf{E}]_{uv:} = \mathbf{e}_{uv}$. Additionally, the graph \mathcal{G} can be defined as a *geometric graph* if each node v represents a point on the 3D Euclidean space and their connections have a notion of distance associated with them. In this case, the augmented graph is given by $\mathcal{G} = \{\mathcal{V}, \mathcal{E}, \mathbf{X}, \mathbf{E}, \mathbf{R}\}$ where $\mathbf{R} \in \mathbb{R}^{N \times 3}$ stores the 3D coordinates of the nodes. Often, \mathcal{E} is built by thresholding the distance between the neighboring nodes using a radius cutoff (r_c) specific to a given downstream application. Particularly,

$$\mathcal{E} = \{(u, v) \mid u \neq v, \|\mathbf{r}_u - \mathbf{r}_v\| < r_c\}$$

where $[\mathbf{R}]_{u:} = \mathbf{r}_u$. Ex., for atomistic graphs such as Fig. 1, the radius cutoff is carefully chosen to capture chemical and physical properties including specific bond lengths (1–2 Å), non-bonded interactions like van der Waals forces (3–5 Å) and metal-ligand interactions (5–6 Å). Leveraging the connectivity structure of graphs to generate useful mathematical abstractions has been the fundamental motivation in developing the theory of graph machine learning and specifically GNNs.

2.2 Long Range Interactions

The long-range interaction (LRI) effects in molecules arise from fundamental physical forces—electrostatics (multipole interactions), induction (polarization), and dispersion

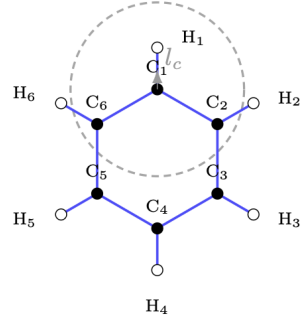


Fig. 1: Geometric atomistic graph with cutoff r_c .

(London forces)—which decay only as inverse powers of the interatomic distance and therefore persist well beyond the typical neighbor cutoffs used in local models (Stone 2013; Israelachvili 2011; London 1937b). To formalize LRIs, we consider two complementary notions of distance between atoms u and v : the shortest-path (graph) distance $d_G(u, v)$ on the atomistic bond graph, and the Euclidean distance $r_{uv} = \|\mathbf{r}_u - \mathbf{r}_v\|_2$ in 3D space (Trinajstić 1992). An interaction is deemed *long-range* for a given node u if there exists at least one atom v whose contribution to the target property cannot be captured by information within a small k -hop neighborhood:

$$\exists v : d_G(u, v) \gg k \quad \text{or} \quad r_{uv} \gg r_c \quad \text{but} \quad \text{influence}(v \rightarrow u) \not\approx 0.$$

These two distances capture different manifestations of nonlocality: in folded or spatially compact conformers, d_L can be small even when d_G is large, producing through-space, nonbonded contacts; in extended or rigid systems, d_G may be small while d_L is large. Related concepts appear in protein *contact order*, which measures spatial proximity despite large sequence (graph) separation (Plaxco et al. 1998).

Physically, such atom–atom relationships can be grouped into interactions between two molecular *fragments* A and B containing u and v , respectively. At large separations, the interaction energy between A and B admits a multi-pole–polarization–dispersion decomposition:

$$E_{\text{int}}(R) \approx E_{\text{elst}}(R) + E_{\text{ind}}(R) + E_{\text{disp}}(R) + \dots,$$

where R is the Euclidean separation between the fragments’ centers (or a representative interatomic distance). Electrostatics is described by a multi-pole expansion, where the potential from a monopole decays as R^{-1} , from a dipole as R^{-2} , and in general from a multi-pole of order ℓ as $R^{-(\ell+1)}$, with the corresponding fields decaying one power faster (e.g., a dipole field as R^{-3}) (Stone 2013). Induction arises when the field of one fragment polarizes the other; for isotropic fragments, the orientationally averaged induction energy scales as R^{-6} (Stone 2013; Israelachvili 2011). Dispersion, due to correlated electron fluctuations, has a leading attractive term $-C_6/R^6$ with higher-order corrections $-C_8/R^8$, $-C_{10}/R^{10}$ (London 1937b; Stone 2013), and in the retarded Casimir–Polder regime scales as R^{-7} (Casimir and Polder 1948a). By contrast, short-range exchange (Pauli) repulsion decays exponentially and is described in frameworks such as SAPT and in overlap-based models (Jeziorski et al. 1994; Born and Mayer 1932).

2.3 MPNN Architectures

An MPNN architecture (Battaglia et al. 2018; Zhou et al. 2020; Wu et al. 2021) is a deep learning architecture that performs convolution-like operations on node features by exploiting the irregular connectivity patterns inherent in graph-structured data. A K –layer MPNN is given by,

$$\bar{\mathbf{H}}^{(k)} = \bigoplus (\phi(\mathbf{H}^{(k-1)}, \omega_k), \mathcal{E}, \mathbf{E}) \quad \forall k \in \{1, \dots, K\} \quad (1)$$

$$\mathbf{H}^{(k)} = \Psi(\bar{\mathbf{H}}^{(k)}, \mathbf{H}^{(k-1)}) \quad (2)$$

where $\mathbf{H}^{(k)} \in \mathbb{R}^{N \times d_k}$ are the node representations after k MPNN layers and $\mathbf{H}^{(0)} = \mathbf{X}$. $\phi(\cdot, \omega)$ denotes a linear transformation of the node features and the trainable weights ω_k are shared by all nodes in the graph at a given layer k . The aggregator \oplus generates node representations by combining information from corresponding local neighborhoods $\mathcal{N}_u = \{v \mid v \in \mathcal{V}, v \neq u, (u, v) \in \mathcal{E}\}$, while leveraging the edge attributes \mathbf{E} , if available. An arbitrary MPNN layer is shown in Fig. 2. Depending on the specific functional form of \oplus , a broad class of MPNN models (Kipf and Welling 2017; Hamilton et al. 2017; Gilmer et al. 2017; Veličković et al. 2018; Xu et al. 2019; Battaglia et al. 2018; Wu et al. 2021; Zhou et al. 2020) have been proposed. Ψ is a node update function such as a multi-layer perceptron (MLP) or gated recurrent unit (GRU). The MPNN output $\mathbf{H}^{(K)}$ stores the full set of node representations that are used for node-level downstream tasks. For graph-level tasks, several pooling operations (i.e., min, max, sum, average) have been employed to convert $\mathbf{H}^{(K)}$ into a dense graph-level representation.

In atomistic modeling applications, it is crucial to incorporate geometric information such as atomic coordinates, interatomic distances, and angles into the message-passing process. To this aim, chemistry or physics-driven MPNN architectures like SchNet (Schütt et al. 2018a), DimeNet (Klicpera et al. 2020d), and EGNN (Satorras et al. 2021) extend standard MPNNs by encoding continuous geometric features as edge attributes, applying distance-based filters, or enforcing equivariance under Euclidean transformations. These chemistry-inspired MPNN architectures construct geometric embeddings by:

- Extracting pairwise distances and triplet bond angles for nodes u and v with coordinates $\mathbf{r}_u, \mathbf{r}_v \in \mathbb{R}^3$,

$$r_{uv} = \|\mathbf{r}_u - \mathbf{r}_v\|, \quad \theta_{uvw} = \angle(\mathbf{r}_v - \mathbf{r}_u, \mathbf{r}_w - \mathbf{r}_u), \quad (3)$$

- Embedding these geometric quantities into a latent edge representation:

$$\bar{\mathbf{e}}_{uv} = \phi_l(r_{uv}) + \sum_{w \in \mathcal{N}_u \setminus \{v\}} \phi_a(\theta_{uvw}), \quad (4)$$

where ϕ_r and ϕ_a are learnable radial and angular embedding functions, respectively.

- Computing messages from neighbor v to node u at any layer k of the K –layer model as:

$$\mathbf{m}_{u \leftarrow v}^{(k)} = \xi(\mathbf{h}_u^{(k-1)}, \mathbf{h}_v^{(k-1)}, \bar{\mathbf{e}}_{uv}), \quad (5)$$

where ξ is a trainable message function that conditions on both node features and geometry-aware edge features and $[\mathbf{H}]_v = \mathbf{h}_v$.

- Aggregating node features using incoming messages:

$$\mathbf{h}_u^{(k)} = \Psi\left(\mathbf{h}_u^{(k-1)}, \bigoplus_{v \in \mathcal{N}(u)} \mathbf{m}_{u \leftarrow v}^{(k)}\right), \quad (6)$$

For graph-level prediction tasks, the final node states $\mathbf{H}^{(K)}$ are aggregated via pooling layers. These approaches allow the network to remain sensitive to spatial relationships while respecting physical symmetries, thereby improving its ability to learn from data where geometry directly governs the target properties. While MPNNs are sufficiently expressive to modeling complex, inter-connected data and offer better generalization capabilities than non-graph ML models (with exceptions; see Section 2), critical challenges still remain unaddressed in terms of large-scale data handling, model scalability and systematic comparison between different graph-based DL architectures.

2.4 Invariance and Equivariance in MPNN Architectures

In geometric GNNs, *invariance* means that the GNN prediction is unchanged under translations, rotations, or reflections of the input, whereas *equivariance* means that the prediction transforms in the same way as the input under a symmetry group such as $E(n)$ or $SE(3)$. For rigid motions $(R, \mathbf{t}) \in SE(3)$ acting on \mathbf{R} row-wise, invariance means $f(R\mathbf{R} + \mathbf{t}) = f(\mathbf{R})$, equivariance means $g(R\mathbf{R} + \mathbf{t}) = Rg(\mathbf{R})$. Generally, $E(n)/SE(3)$ –equivariance is required when the target is directional or tensorial—e.g., atomic forces, dipole moments, and vector fields—where architectures like EGNN, $SE(3)$ -Transformer, PaiNN, and NequIP are designed to respect these symmetries (Satorras et al. 2021; Fuchs et al. 2020; Schütt et al. 2021; Batzner et al. 2022). For invariant scalar properties (e.g., total energy, band gap, class labels), enforcing invariance and injecting *invariant geometric biases*—pairwise distances and angular/triplet features—typically suffices; SchNet uses continuous filters over interatomic distances, while DimeNet/DimeNet++ augment with angles via spherical Bessel and spherical harmonic bases (Schütt et al. 2018a; Klicpera et al. 2020c,a). Note that even invariant energy models can yield *equivariant* forces by taking analytic gradients of the predicted energy with respect to the coordinates of the atoms’ nuclei, though explicitly equivariant models often improve accuracy and sample efficiency for a more general class of vector/tensor target properties (Schütt et al. 2018a; Batzner et al. 2022; Satorras et al. 2021).

2.5 Limitations of Message-Passing

A straightforward technique to capture LRI in MPNNs is to deepen the DL architecture to ensure that the effective receptive field covers the whole graph around the node being processed. This approach, however, entails some major shortcomings:

Over-smoothing. Stacking many neighborhood-averaging layers repeatedly applies a (normalized) smoothing operator on the graph. As depth grows, node features from the same connected component can become nearly indistinguishable, hurting discriminability of the model. Essentially, the *low-pass* nature of the aggregation operation filters out most of the high-frequency discriminative information with increase in depth of the model. This phenomenon—*over-smoothing*—has been analyzed both empirically via Laplacian smoothing interpretations and theoretically via asymptotic collapse of node embeddings (Li et al. 2018b; Oono and Suzuki 2020b).

Over-squashing (bottlenecks and curvature). Even when K is large enough to cover long graph distances, information arriving from exponentially many k -hop nodes may be *squashed* into fixed-width messages that must traverse narrow graph cuts (small edge separators). This *over-squashing* bottleneck limits long-range dependency modeling in MPNNs (Alon and Yahav 2021b). Recent theory connects over-squashing to discrete curvature: negatively curved (tree-like) regions expand neighborhoods exponentially while admitting small cuts, exacerbating information congestion.

Therefore, local message-passing is often inadequate in capturing LRI, especially for large-sized atomistic graphs that require a larger receptive field to cover the whole graph around each node.

2.6 GT Architectures

In recent years, graph-based DL has successfully ventured beyond MPNN models – which are inherently localized information aggregators and treat a graph as the combination of localized parts – and leveraged DL models that have a global scope and can process the graph as a whole. Specifically, a GT (Dwivedi and Bresson 2020; Kreuzer et al. 2021; Ying et al. 2021a) is a DL architecture that uses the *self-attention* mechanism (Vaswani et al. 2017). Note that the term “Graph Transformer” can also refer to a specific global attention architecture (Dwivedi and Bresson 2020). However, in this work we use it as a descriptor for the general attention-based model class. In this framework, each node aggregates information from all other nodes in the graph via a learned attention mechanism, enabling the learning of both local and global dependencies beyond fixed-hop neighborhoods. The *multi-head attention* (MHA) mechanism allows the model to jointly attend to information from different representation subspaces, thereby enhancing expressiveness and robustness. At an arbitrary layer m of an M –layered GT, the node embedding matrix $\mathbf{H}^{m-1} \in \mathbb{R}^{N \times d_{m-1}}$ is projected by the attention heads into query, key, and value spaces:

$$\mathbf{Q}^m = \mathbf{H}^{m-1} \mathbf{W}_Q^m, \quad \mathbf{K}^m = \mathbf{H}^{m-1} \mathbf{W}_K^m, \quad \mathbf{V}^m = \mathbf{H}^{m-1} \mathbf{W}_V^m, \quad (7)$$

where $\mathbf{W}_Q^m, \mathbf{W}_K^m, \mathbf{W}_V^m \in \mathbb{R}^{d_{m-1} \times d_m}$ are learnable weight matrices. The scaled dot-product attention for one head is computed as:

$$\text{AttHead}(\mathbf{Q}^m, \mathbf{K}^m, \mathbf{V}^m) = \text{softmax} \left(\frac{\mathbf{Q}^m \mathbf{K}^{m\top}}{\sqrt{d_m}} \right) \mathbf{V}^m. \quad (8)$$

where softmax is applied independently on each row. For B heads, the outputs are concatenated and linearly projected:

$$\text{MultiHead}(\mathbf{Q}^m, \mathbf{K}^m, \mathbf{V}^m) = \text{Concat}(\text{AttHead}_1, \dots, \text{AttHead}_B) \mathbf{W}_O^m, \quad (9)$$

where $\mathbf{W}_O^m \in \mathbb{R}^{Bd_m \times d_m}$ is a learnable projection matrix. By integrating *structural* and *positional encodings*, the GT effectively incorporates relational inductive biases, making it applicable to diverse tasks such as node classification, link prediction, and graph-level prediction. We will discuss this in more detail in Section 2.

2.7 HydraGNN

HydraGNN (Lupo-Pasini et al. 2022b) is a multi-task learning MPNN architecture designed to simultaneously predict both global (graph-level) and atomic (node-level) material properties from atomic structure inputs. HydraGNN efficiently integrates DDP for large-scale atomistic datasets (sizes can range from a few hundred thousand to a few millions) with a broad set of MPNN layers as base learners that can be distributed across distributed computing resources with model parallelism. HydraGNN employs shared MPNN layers to extract features common across all target properties, followed by multiple task-specific output decoding heads for property-specific learning via hard parameter sharing of the MPNN layers. Each task is associated with its own loss function, and the global objective is defined as a weighted sum of individual task losses. HydraGNN supports seamless switching across SOTA message-passing, geometric and equivariant GNN architectures, thereby allowing for efficient architecture search through integrated HPO. The effectiveness of this framework both in terms of prediction accuracy and scalability has been well established through rigorous evaluation on multiple material science applications Lupo-Pasini et al. (2022a,b); Choi et al. (2022); Baker et al. (2023); Lupo-Pasini et al. (2023, 2025a,b).

2.8 Hybrid GNN Architectures

General, Powerful, Scalable (GPS) framework introduces a hybrid graph architecture that combines the strengths of MPNNs and GTs. At each layer, GPS¹ integrates local neighborhood aggregation (via MPNNs, which capture edge-level and structural information) with global multi-head attention (which enables long-range dependencies) – by leveraging positional and structural encodings, – to overcome the expressivity limits of standard GNNs (Rampásek et al. 2022). Effectively, this method enables aggregation of global information in addition to local messages at each node in each layer of

¹**Complexity.** Full self-attention over N nodes (dense $N \times N$ attention) costs $\mathcal{O}(N^2)$ time and memory per layer; message passing scales with $\mathcal{O}(|\mathcal{E}|)$ (often $\mathcal{O}(N)$ on bounded-degree/radius graphs). GPS blends both, yielding $\mathcal{O}(|\mathcal{E}| + N^2)$ per layer.

the architecture. Thus, it obviates the necessity (and corresponding pitfalls) of deeper GNN architectures. Formally, the ℓ^{th} GPS layer is given by:

$$\mathbf{X}^{\ell+1}, \mathbf{E}^{\ell+1} = \text{GPS}^\ell(\mathbf{X}^\ell, \mathbf{E}^\ell, \mathcal{E}) \quad (10)$$

where,

$$\hat{\mathbf{X}}_M^{\ell+1}, \mathbf{E}^{\ell+1} = \text{GNN}^\ell(\mathbf{X}^\ell, \mathbf{E}^\ell, \mathcal{E}), \quad (11)$$

$$\hat{\mathbf{X}}_T^{\ell+1} = \text{MHA}^\ell(\mathbf{X}^\ell), \quad (12)$$

$$\mathbf{X}^{\ell+1} = \text{MLP}^\ell(\hat{\mathbf{X}}_M^{\ell+1} + \hat{\mathbf{X}}_T^{\ell+1}). \quad (13)$$

Building on these capabilities, GPS++ (Masters et al. 2023b) refines the balance between local and global processing for atomistic property prediction. GPS++ emphasizes a strong, well-tuned message passing module, complemented by biased self-attention informed by structural and geometric priors, such as shortest-path and 3D distance embeddings. Through extensive ablations, GPS++ shows that much of its performance can be retained even without global self-attention, highlighting that expressive message passing remains highly competitive, particularly when 3D positional data is absent.

In spite of the synergistic combination of local and global information, the GPS and its enhancements have been successfully employed only on a limited class of scientific materials (Rampásek et al. 2022; Masters et al. 2023b) and in smaller quantity. Moreover, the baseline results were obtained using a limited set of MPNN architectures and no equivariant models were compared. In addition, it was shown that with proper hyper-parameter tuning, MPNN models could still outperform GT models and GPS (Tönshoff et al. 2023). Therefore, the possibility of building an end-to-end framework for handling large-quantities of scientific materials from a varied set of application areas, using a broad class of MPNN models in tandem with global attention – with best models selected using automated hyper-parameter optimization (HPO) – remains an open problem for the research community.

3 Method

We developed an integrated *MPNN and Global Attention* framework within HydraGNN that allows users to seamlessly switch across independent model configurations that offer various techniques to aggregate information across graph data. Figure 3 shows the different model configurations options provided by the newly expanded HydraGNN framework, toggled by switches S1 and S2.

1. By opening both S1 and S2, the model resembles the HydraGNN (Lupo-Pasini et al. 2022b) architecture with its core functionalities such as DDP for large-scale datasets and a large selection of MPNN models – both invariant and equivariant – to choose from.
2. By closing S2 when S1 is open, we obtain an augmented version of HydraGNN where additional chemical and topological attributes are computed as a pre-processing

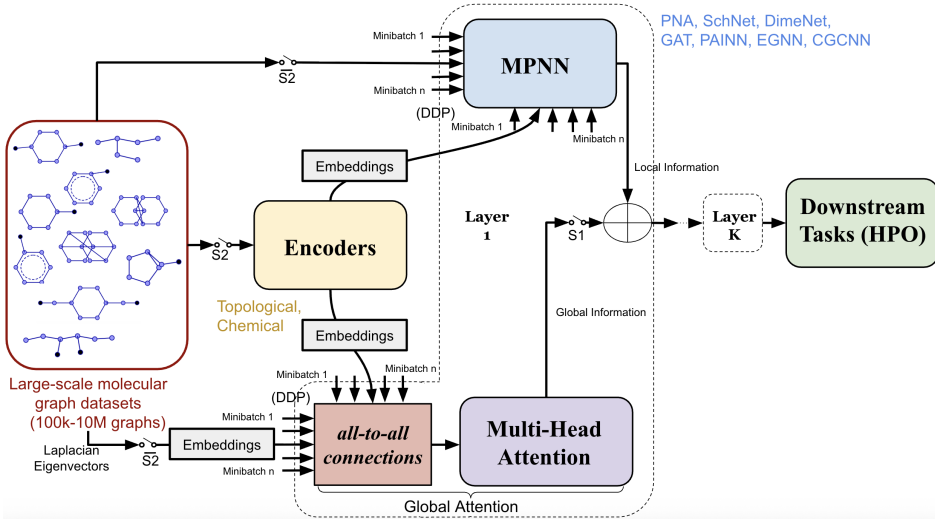


Fig. 3: Flow diagram depicting the computational steps in our proposed framework. It depicts a K -layered model. **Each block operates parallelly on individual graphs.** Four independent pipelines are denoted by configurations of the switches $S1$ and $S2$. Ex., if $S1$ and $S2$ are both open, HydraGNN pipeline is obtained. And, if $S1$ and $S2$ are both closed, global attention module is fused with local message-passing module while encoders provide domain-specific and positional information to both modules. Input features are embedded to suitable subspaces before feeding to the learnable modules. Output of layer K is used for downstream tasks through hyper-parameter optimization.

step for each graph through an encoder module, which are first embedded using learnable transformations to a user-defined subspace and then leveraged by the MPNN module for the final downstream task.

3. Further, by opening $S2$ and closing $S1$, the model resembles the GPS (Rampásek et al. 2022) architecture embedded within the HydraGNN pipeline. The suitably embedded *laplacian eigenvectors* are used as positional encodings for the Global-Attention module. This scheme essentially combines the advantages of both models within a single end-to-end setup.
4. Finally, by closing both $S1$ and $S2$, we obtain a fully integrated model that combines the encoder, embedding, global attention and MPNN modules, together with DDP for large-scale data handling. We note that this model is in principle similar to GPS++ (Masters et al. 2023b). However, we do not use graphomer-style encodings and moreover, we use a broader class of MPNNs to aggregate local information than the aforementioned work.

Crucial to the operation of this framework is the encoder module that pre-computes certain fundamental chemical properties of the molecules (at the level of the constituent atoms and the bonds) and topological properties of the corresponding graphs.

Besides being useful for the Global-Attention module (that does not use the underlying local connectivity structure of the atomistic graph) to distinguish between nodes and edges of specific chemical types and topological structures and positions in the graph, these features also allow the MPNN modules to leverage the existing information that would otherwise be computed implicitly through message passing for a given downstream task.

3.1 Encoders

Each atomistic graph is augmented with 3D coordinates of the constituent atoms, if the geometric information is available. The final model input for a graph consists of (i) raw atom/bond attributes, (ii) chemically informed per-atom descriptors, (iii) structural and positional encodings on nodes and edges, and (iv) simple geometric edge attributes. All feature blocks are standardized (zero mean, unit variance) per dataset split.

Atoms. For datasets that provide rich atom encodings (e.g., OGB (Hu et al. 2020a) mol tasks), we adopt the standard 9-dimensional atom feature vector covering atomic number, degree, formal charge, number of attached hydrogens, chirality, hybridization, aromaticity, and ring membership.² For QM9 (Ramakrishnan et al. 2014a; Ruddigkeit et al. 2012a) we use the atomic number Z as the base node attribute, while for the NIAD MoF crystal dataset (Burner et al. 2025) we use a two-channel node attribute $[Z, q^{(\text{partial})}]$, where $q^{(\text{partial})}$ is an (available) per-atom partial charge.

Chemically informed descriptors (CE). In addition to the raw attributes above, we compute a 15-dimensional per-atom descriptor vector using the following Mendeleev atomic properties: atomic weight, group, period, block (s/p/d/f), valence electron count, covalent radius, van der Waals radius, Pauling and Allen electronegativities, electron affinity, first ionization energy, melting point, boiling point, density, and atomic volume. This descriptor matrix is standardized and concatenated as a separate channel available to the encoder.

Topological encodings (TE). We add two complementary, position- and structure-aware encodings: (i) **Node PE**: a 9-feature stack of classic centrality/structure measures—degree, closeness, betweenness, eigenvector centrality, PageRank, local clustering coefficient, k -core number, harmonic centrality, and eccentricity—computed on the undirected atomistic graph and standardized. (ii) **Edge PE**: a 4-feature vector per edge comprising edge betweenness, Jaccard coefficient, Adamic–Adar score, and preferential attachment, standardized. In addition, we include **Laplacian eigenvector positional encodings (LPE)**: the top k eigenvectors of the (symmetrized) graph Laplacian, which we compute once per graph (hyperparameter k set in the config) and standardize.

Bonds and geometry. Bond features are customized based on the specific dataset used. For instance, OGB (Hu et al. 2020a) supplies bond type, stereochemistry, conjugation information, while ZINC (Irwin and Shoichet 2005a) and QM9 (Ramakrishnan et al. 2014a; Ruddigkeit et al. 2012a) provide discrete bond attributes. For 3D structure, when coordinates are available we build the graph either from the dataset’s bond list or, for crystals, by a radius cutoff in Cartesian space, and attach the *pairwise*

²Edge features from OGB include bond type, stereochemistry, and conjugation.

interatomic distance $\|\mathbf{r}_i - \mathbf{r}_j\|$ as a continuous edge attribute. No explicit angle or dihedral features are used in our current experiments; instead, angular information is captured implicitly through message passing over the distance-augmented graph and the positional encodings.

Therefore, given a graph with N nodes and $|\mathcal{E}|$ edges, the model consumes: $\mathbf{X} \in \mathbb{R}^{N \times p}$ (raw atom features), $\mathbf{C} \in \mathbb{R}^{N \times 15}$ (Mendeleev descriptors), $\mathbf{P} \in \mathbb{R}^{N \times 9}$ (node topological encodings), $\mathbf{L} \in \mathbb{R}^{N \times d_l}$ (LPE), $\mathbf{E} \in \mathbb{R}^{|\mathcal{E}| \times f}$ (raw bond features and/or distances), and $\mathbf{G} \in \mathbb{R}^{M \times 4}$ (edge topological encodings). Further, if the model is equivariant, it also consumes the 3D coordinates $\mathbf{R} \in \mathbb{R}^{M \times 3}$. All channels are standardized before training, and samples with invalid values in computed encodings are discarded, which typically constitutes a negligible amount for each dataset.

3.2 Embeddings

We introduce a lightweight embedding module that unifies raw node/edge attributes with multiple classes of encodings and maps node and edge attributes to suitable subspaces of user-chosen dimensionality. Particularly, this module is employed for all schemes except the vanilla HydraGNN pipeline (Scheme 1), which operates directly on \mathbf{X} and possibly \mathbf{E} . It either embeds a combination of \mathbf{X} and \mathbf{L} on nodes and \mathbf{E} on edges if only Global-Attention is activated (Scheme 3) while schemes 2 and 4 require embedding all the available encodings to a common subspace.

Node embedding. To build the input node embeddings for schemes 2, 3 and 4, we form a node input tensor by concatenation of the available encodings

$$\mathbf{Z}_{\text{node}} = [\mathbf{X} \parallel \mathbf{L} \parallel \mathbf{P} \parallel \mathbf{C}] \in \mathbb{R}^{N \times d_{\text{node}}^{\text{in}}},$$

where absent tensors are simply omitted depending on the particular scheme being employed. A single linear projection with no bias maps to a hidden width d_h :

$$\mathbf{H} = \mathbf{Z}_{\text{node}} \mathbf{W}_{\text{node}}, \quad \mathbf{W}_{\text{node}} \in \mathbb{R}^{d_{\text{node}}^{\text{in}} \times d_h}.$$

This preserves alignment across nodes while minimizing parameters. For Scheme 1, the module devolves to an identity on node encodings and returns \mathbf{X} unchanged, enabling plug-and-play ablations.

Edge embedding. When using MPNNs that are designed to handle edge features, we construct edge inputs via one of two modes: (1) \mathbf{G} is used directly when encoders are employed or (2) if Global-Attention is activated but encoders are not used, for each edge (u, v) with indices (i, j) , we compute the absolute difference of node-wise LPEs,

$$\mathbf{r}_{(u, v)} = |\mathbf{L}_{i:} - \mathbf{L}_{j:}| \in \mathbb{R}^{d_\ell},$$

which is permutation-invariant and captures a simple notion of spectral displacement. Raw edge attributes \mathbf{E} , if available, are concatenated with the encodings. The resulting edge tensor

$$\mathbf{Z}_{\text{edge}} \in \mathbb{R}^{E \times d_{\text{edge}}^{\text{in}}}$$

is linearly projected (no bias) to an edge embedding $\mathbf{A} \in \mathbb{R}^{|\mathcal{E}| \times d'_e}$ and used to replace the input edge attributes $\mathbf{E} = \mathbf{A}$ to the model. For Scheme 1, the raw edge features are directly passed to the model. This lets downstream convolutions remain agnostic to the encoding sources while benefiting from unified edge representations.

In terms of complexity of the embedding operations, the dominant costs are two dense multiplications:

$$\mathcal{O}(N d_{\text{node}}^{\text{in}} d_h) \quad \text{and} \quad \mathcal{O}(|\mathcal{E}| d_{\text{edge}}^{\text{in}} d'_e),$$

plus an $\mathcal{O}(|\mathcal{E}| d_\ell)$ LPE-difference when encoders are disabled. Since the MPNNs and Global-Attention already perform $\mathcal{O}(N^2)$ operations, the overall complexity of the model is unaffected by the additional embedding layers. Further, we note the following main advantages of our method: (i) *Single-projection fusion*. Using one bias-free linear for nodes and edges each reduces parameters and avoids redundant per-channel MLPs while letting the backbone allocate depth where it matters. (ii) *Decoupled toggles*. The four flags enable clean ablations: raw features only; raw+LPE; raw+TE(+CE); and edge-aware vs. node-only. (iii) *Spectral relativity*. The LPE-difference path offers a cheap, sign-invariant relational signal when explicit RPEs are unavailable.

3.3 Model Training

Training is performed under the HydraGNN framework with hyperparameter optimization (HPO) driven by DeepHyper (Balaprakash et al. 2018; Egelé et al. 2023). Let \mathcal{H} denote the search space of hyperparameters (e.g., learning rate, hidden width d_h , edge width d'_e , dropout). For each candidate $h \in \mathcal{H}$, we train a model $f_{\theta,h}$ for T epochs by minimizing the training loss

$$\mathcal{L}(\theta; h) = \frac{1}{|\mathcal{D}_{\text{train}}|} \sum_{(x,y) \in \mathcal{D}_{\text{train}}} \ell(f_{\theta,h}(x), y),$$

with ℓ typically chosen as squared error. Validation performance $\mathcal{L}_{\text{val}}(h)$ determines the best configuration

$$h^* = \arg \min_{h \in \mathcal{H}} \mathcal{L}_{\text{val}}(h).$$

We then re-train f_{θ,h^*} for an extended budget $T' \gg T$, subject to early stopping after p consecutive epochs without improvement in \mathcal{L}_{val} . Model checkpointing ensures persistence of parameters θ_t at each epoch, providing both recovery and reproducibility.

The cost of the HPO phase scales as

$$\mathcal{O}(|\mathcal{H}| T C_{\text{epoch}}),$$

where C_{epoch} denotes the cost of a single training epoch on the dataset. For graph data with N nodes and $|\mathcal{E}|$ edges per sample, we approximate

$$C_{\text{epoch}} = \mathcal{O} \left(\sum_{(x,y) \in \mathcal{D}_{\text{train}}} (Nd_h^2 + |\mathcal{E}|d_e'^2) \right),$$

where d_h is the hidden node width and d_e' the edge embedding width (cf. Section 3.2). After HPO, the re-training phase requires $\mathcal{O}(T' C_{\text{epoch}})$.

4 Experiments

Our experimental protocol evaluates the proposed framework across a broad suite of open-source atomistic datasets. For each dataset, we adopt the official train/validation/test split when provided; otherwise, we apply an 80%/10%/10% splitting. For every dataset and learning scheme, we perform hyperparameter optimization (HPO) to maximize the validation objective, select the best configuration, and then report that configuration on the held-out test set. Task-appropriate metrics are used throughout: mean absolute error (MAE) for regression targets, classification accuracy for OGB-PPA, and mean average precision (mAP) for OGB-PCBA. This procedure yields a standardized, reproducible comparison across datasets and provides an unbiased estimate of generalization to unseen graphs.

4.1 Datasets

We evaluate on 7 datasets spanning atomistic and biochemical graph regimes (Table 1). The collection comprises $\sim 4.21\text{M}$ graphs with mean sizes from ~ 18 to ~ 243 nodes, covering small molecules (QM9, ZINC, OGB-PCQM) and larger, more complex structures (TMQM, NIAID, OGB-PPA). Supervision includes four graph-level regression targets—free energy at 298.15 K (QM9), constrained solubility (ZINC), dispersion energy (TMQM), and the HOMO–LUMO gap (OGB-PCQM)—one node-level regression target (partial charges in NIAID), and two graph-level classification benchmarks: multi-class accuracy on OGB-PPA and multi-label mAP on OGB-PCBA.

We set the LPE dimensionality d_ℓ to the number of smallest nonzero Laplacian eigenvectors that are consistently available across graphs in each dataset; a small fraction of graphs with fewer than d_ℓ nontrivial eigenvectors are omitted. Table 1 lists d_ℓ per dataset.

QM9 provides equilibrium geometries and a standardized suite of quantum-chemical properties for small organic molecules curated from the GDB chemical universe [Ramakrishnan et al. \(2014b\)](#); [Ruddigkeit et al. \(2012b\)](#). Nodes encode atomic number; edges correspond to covalent bonds with one-hot bond type (single/double/triple/aromatic). QM9 offers 19 regression targets: Dipole moment, Isotropic polarizability, Highest occupied molecular orbital energy, Lowest unoccupied molecular orbital energy, Gap between HOMO and LUMO, Electronic spatial extent, Zero point vibrational energy, Internal energy at 0K, Internal energy at 298.15K, Enthalpy at 298.15K, Free energy at 298.15K, Heat capacity at 298.15K, Atomization energy at

Table 1: Graph dataset summary and LPE dimensionality.

Dataset	Avg. # Nodes	# Graphs	# lapPE (d_ℓ)
QM9	~18	130k	2
ZINC	~23	250k	5
TMQM	~120	100k	6
NIAID	~200	130k	6
OGB-PCQM4Mv2	~20	3M	4
OGB-PPA	~243	158k	5
OGB-molPCBA	~26	438k	5

0K, Atomization energy at 298.15K, Atomization enthalpy at 298.15K, Atomization free energy at 298.15K, Rotational constant A, Rotational constant B, Rotational constant C. In our experiments, we predict **Free energy at 298.15K**.

ZINC is a freely available repository of purchasable small molecules prepared in 3D, protonation, and tautomeric states for virtual screening; we reference both the original release and ZINC15 [Irwin and Shoichet \(2005b\)](#); [Sterling and Irwin \(2015\)](#). Nodes represent heavy atoms with features including atomic number (atom type), chirality, atomic degree, formal charge, number of attached hydrogens, number of radical electrons, hybridization state, aromaticity, and ring membership. Edges are covalent bonds with bond order (single/double/triple/aromatic), stereo configuration (e.g., cis/trans), and a binary conjugation indicator. The task is to regress over graph-level **Constrained Solubility** (logP).

TMQM comprises quantum-optimized geometries and electronic properties for a large, structurally diverse set of mononuclear transition-metal complexes from the Cambridge Structural Database [Balcells and Skjelstad \(2020\)](#). We construct geometric graphs using a 5.0Å radius cutoff. Node features include atomic number, formal charge, atomic valence indices, and 3D coordinates; edges carry real-valued Euclidean distances for atom pairs within the cutoff. The dataset provides 11 targets (e.g., molecular charge, spin, metal coordination degree, electronic energy, dispersion energy, dipole moment, natural charge at the metal center, HOMO–LUMO gap, HOMO/LUMO energies, polarizability); here we focus on graph-level **Dispersion Energy** regression.

NIAID contains experimental and computational metal-organic frameworks with REPEAT DFT-derived partial charges and precomputed descriptors, accessed via the NIAID Data Discovery Portal [Burner et al. \(2022a,b\)](#). Graphs are built with a 5.0Å radius cutoff. Node features are atomic numbers; edges encode Euclidean distances. The task is node-level regression of per-atom **Partial Charges**.

OGB-PCQM (PCQM4Mv2) defines prediction of the DFT HOMO-LUMO gap from 2D molecular graphs curated from PubChemQC, with standardized splits and evaluation protocols for large-scale graph learning [pcq \(2022\)](#); [Hu et al. \(2021\)](#); [Nakata and Shimazaki \(2017\)](#).

OGB-PCBA is OGB’s adaptation of the MoleculeNet molPCBA suite derived from PubChem BioAssay, providing many binary endpoints and strong baselines for evaluating classifier calibration and transfer [Hu et al. \(2020b\)](#); [Wu et al. \(2018\)](#). We use this dataset for graph-level multi-label classification.

Featurization for OGB-PCQM and OGB-PCBA. Both datasets share the same molecular featurization. Each node is annotated with its atomic number, chirality type (e.g., R/S stereocenter), atomic degree, formal charge, number of attached hydrogens, number of radical electrons, hybridization state, an aromaticity flag, and a ring-membership indicator. Edges correspond to covalent bonds and carry bond type (single/double/triple/aromatic), bond stereo configuration (e.g., cis/trans), and a binary indicator for conjugation.

OGB-PPA consists of protein–protein association (PPA) network neighborhoods spanning many species and taxonomic groups; graphs are derived from STRING associations and labels reflect the source group, enabling evaluation of biological graph generalization [ogb \(2020\)](#); [Szklarczyk et al. \(2019\)](#). We use this dataset for protein-graph classification (37-class, evaluated by accuracy). Nodes represent proteins and do not carry intrinsic atom-level features. Edges encode associations; in our setup, each edge includes a 7-dimensional binary vector indicating evidence channels (e.g., gene co-occurrence, gene fusion events, co-expression), with 1 denoting the presence of the corresponding evidence type.

4.2 Hyperparameter search space (HPO)

We specify a conditional search space over MPNNs and global attention. The space branches on (i) availability of 3D coordinates (`has_pos`), (ii) whether a global attention block is enabled (`global_attn_engine`), and (iii) whether feature encodings are used (`use_encodings`). Discrete ranges denote integer-valued grids; braces `{·}` enumerate categorical options.

Table 2: Model family by coordinate availability.

Condition	<code>mpnn.type</code> options
<code>has_pos</code> = True	{PNA, CGCNN, SchNet, DimeNet, EGNN, PAINN}
<code>has_pos</code> = False	{GAT, GINE, PNA, CGCNN}

Non-equivariant architectures (e.g., PNA, CGCNN) do not consume 3D coordinates (`pos`) and therefore operate identically on 2D graphs. We nevertheless include them in the

HPO search space alongside equivariant models (as shown in Table 2, `has_pos` = True) to enable data-driven selection and to quantify the marginal benefit of explicit geometric information – and SE(3)-equivariance – over standard message passing.

Table 3: Search space when `global_attn_engine` = False.

Hyperparameter	<code>use_encodings=False</code>	<code>use_encodings=True</code>
<code>num_conv_layers</code>	{1, 2, 3, 4, 5, 6}	{1, 2, 3, 4, 5, 6}
<code>global_attn_heads</code>	{0}	{0}
<code>hidden_dim</code>	[4,32]	[16,64]
<code>edge_embed_dim</code>	{0}	{0, 4, 5, 6, 7, 8, 9, 10, 11, 12}

Table 4: Search space when `global_attn_engine` = True.

Hyperparameter	<code>use_encodings=False</code>	<code>use_encodings=True</code>
<code>num_conv_layers</code>	{1, 2, 3}	{1, 2, 3}
<code>global_attn_heads</code>	{2, 4, 8}	{2, 4, 8}
<code>hidden_dim</code>	{8, 16, 24, 32, 40, 48}	{16, 24, 32, 40, 48, 56, 64}
<code>edge_embed_dim</code>	{0, 4, 5, 6, 8, 9, 10, 11, 12}	{0, 4, 5, 6, 7, 8, 9, 10, 11, 12}

Multi-head attention imposes the constraint `hidden_dim` % `global_attn_heads` = 0, i.e., the per-head width $d_{\text{head}} = \text{hidden_dim}/\text{global_attn_heads}$ must be an integer. Accordingly, in Table 4 we restrict `hidden_dim` to multiples of $\text{lcm}(2, 4, 8) = 8$, ensuring every listed `hidden_dim` is compatible with all admissible values of `global_attn_heads` and preventing invalid HPO configurations. When `global_attn_engine` is enabled, we widen the candidate set for `hidden_dim` to admit larger layer widths. This reflects the increased effective receptive field and information aggregation introduced by global attention, allowing the model to be more expressive.

Equivariance toggle. Setting `edge_embed_dim` = 0 uses raw interatomic distance as the sole edge attribute, preserving SE(3)-equivariance for equivariant architectures (e.g., SchNet, DimeNet, EGNN, PAINN). Choosing `edge_embed_dim` > 0 activates the full edge-feature pipeline (e.g., bond/type/auxiliary encodings when available), which generally breaks strict equivariance but can increase expressivity. For the non-equivariant models (GAT, GINE, PNA and CGCNN), `edge_embed_dim` = 0 allows the model to use the raw edge features directly without learnable projections.

4.3 Hardware Setting

All numerical experiments were conducted on the OLCF Frontier supercomputer, the first U.S. exascale system. Frontier is based on the HPE Cray EX architecture and consists of 9,472 compute nodes, each equipped with one AMD EPYC™ 7A53 64-core

CPU and four AMD Instinct™ MI250X GPUs. Each node offers a high-bandwidth memory subsystem with 512 GB of DDR4 memory on the CPU and 128 GB of HBM2e memory across the GPUs, connected via AMD’s Infinity Fabric. Nodes are linked through the HPE Slingshot-11 interconnect, which provides high bandwidth and low latency for large-scale parallel applications. The system is supported by a multi-petabyte Lustre-based parallel file system to enable high-throughput I/O for large-scale simulations.

4.4 Numerical Results

We evaluate four training schemes on all our datasets: (S1) GPS disabled, encoders disabled; (S2) GPS disabled, encoders enabled; (S3) GPS enabled, encoders disabled; (S4) GPS enabled, encoders enabled. For each scheme we report the best HPO trial and its test performance (MSE/MAE/Pearson r as indicated in the plot titles).

4.4.1 ZINC

Tables 5 and 6 indicate that enabling learned encoders without GPS (**S2**) yields the most favorable bias–variance trade-off for this dataset. Relative to the non-encoder baseline (**S1**), MSE decreases by $\sim 62\%$ and MAE by $\sim 37\%$ at a moderate parameter increase (185k vs. 111k). In contrast, activating GPS without encoders (**S3**) reduces parameter count to 62k but substantially degrades accuracy, suggesting that additional global information cannot compensate for weaker token features. Adding GPS on top of encoders (**S4**, 207k parameters) recovers much of the performance lost by **S3** yet remains inferior to **S2**, implying diminishing returns from global information. The parity plots (Figure 4) show tightly clustered residuals with a small number of outliers; **S2** exhibits the highest similarity to the identity with the least dispersion in the high-magnitude regime.

Table 5: ZINC best HPO configuration per scheme

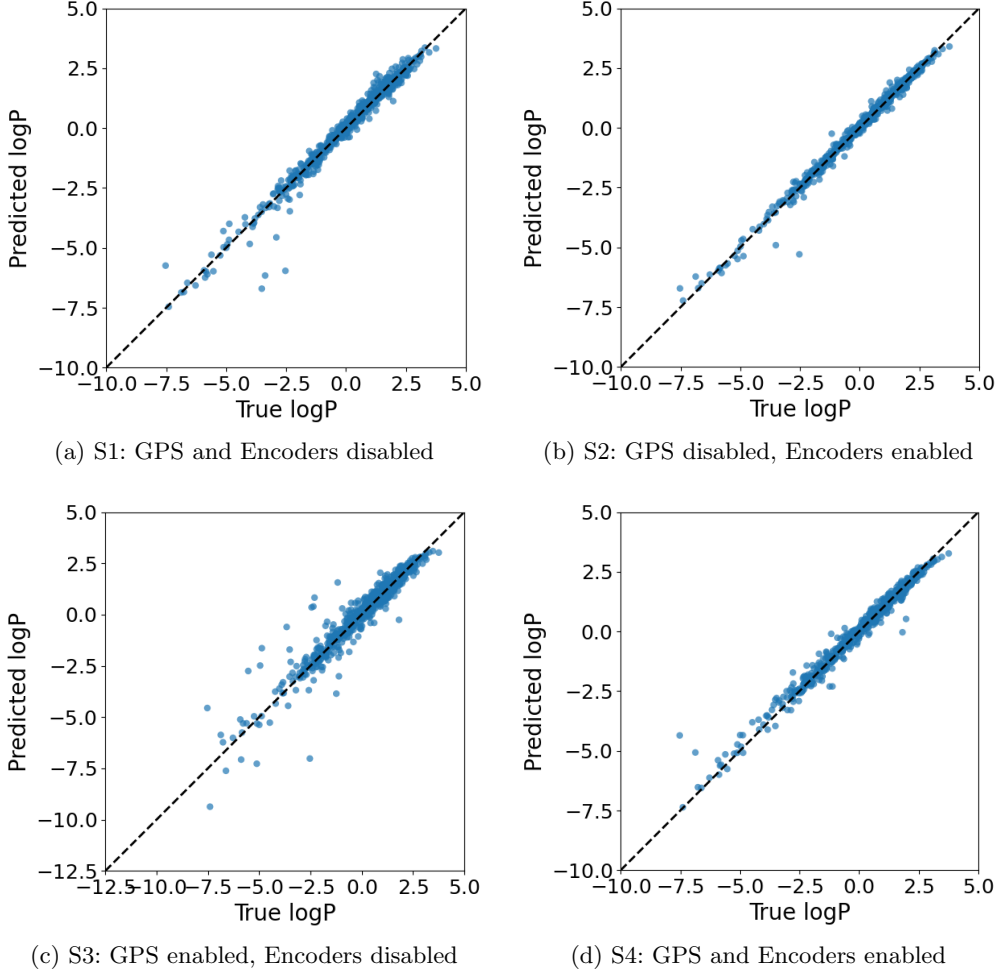
Scheme	MPNN	#Conv	Hidden	EdgeEmb	GPS Heads	#Parameters
S1	PNA	6	32	0	0	111388
S2	PNA	4	46	4	0	185318
S3	PNA	2	32	9	4	62374
S4	PNA	3	48	10	8	207288

4.4.2 QM9

In this case, all schemes achieve $r \approx 1$ (Figure 5), yet error magnitudes depend strongly on architectural choices (Tables 7 and 8). The encoder-augmented PAINN without GPS (**S2**, 82.9k parameters) attains the lowest MSE/MAE, improving upon the compact PAINN baseline (**S1**, 15.1k) by $\sim 20\%$ MSE and $\sim 9\%$ MAE; thus **S1** is highly parameter-efficient but **S2** achieves the best absolute error. GPS-enabled variants (**S3**

Table 6: ZINC test performance by scheme

Scheme	MSE \downarrow	MAE \downarrow	Pearson $r \uparrow$
S1	0.112859	0.197555	0.985365
S2	0.042459	0.125066	0.994298
S3	0.316814	0.326824	0.957194
S4	0.083230	0.181921	0.989287

**Fig. 4:** ZINC parity plots (Predicted vs. True logP) for the best HPO trial per scheme

DimeNet, **S4** PAINN) exhibit markedly larger errors despite near-perfect correlations, consistent with a calibration bias rather than rank ordering failures—visible as a slight slope offset from the identity in Figure 5. The results suggest that for QM9 the quality

of local information and the hidden layer dimension plays an important role, whereas shallow global attention (single-layered) confers no benefit at comparable or even lower model sizes.

Table 7: QM9 best HPO configuration per scheme

Scheme	MPNN	#Conv	Hidden	EdgeEmb	GPS Heads	#Parameters
S1	PAINN	2	15	0	0	15 119
S2	PAINN	2	47	12	0	82 898
S3	DimeNet	2	8	4	2	10 948
S4	PAINN	1	20	10	2	17 992

Table 8: QM9 test performance by scheme

Scheme	MSE \downarrow	MAE \downarrow	Pearson $r\uparrow$
S1	0.002 416	0.036 195	1.000000
S2	0.001934	0.032784	1.000000
S3	4.415 277	1.551 903	0.999 958
S4	7.484 828	2.115 828	0.999 893

4.4.3 TMQM

For this dataset, all configurations lead to similar high quality results (Figure 6), and variations in performance across configurations are very small (Table 10). Notably, the best model (**S2**, PAINN, 63.7k parameters, 1 conv layer) outperforms a substantially larger GPS variant (**S3**, 184.6k) and even a deeper PAINN (**S1**, 65.9k), indicating that increased depth and global heads are unnecessary once sufficiently expressive local encoders are present. The smallest model (**S4**, 27.5k) is close to **S2**, underscoring that this target is amenable to compact networks; additional capacity mainly yields marginal gains.

Table 9: TMQM best HPO configuration per scheme

Scheme	MPNN	#Conv	Hidden	EdgeEmb	GPS Heads	#Parameters
S1	PNA	4	30	0	0	65 933
S2	PAINN	1	59	12	0	63 738
S3	PAINN	3	48	11	8	184 639
S4	PAINN	3	16	12	8	27 486

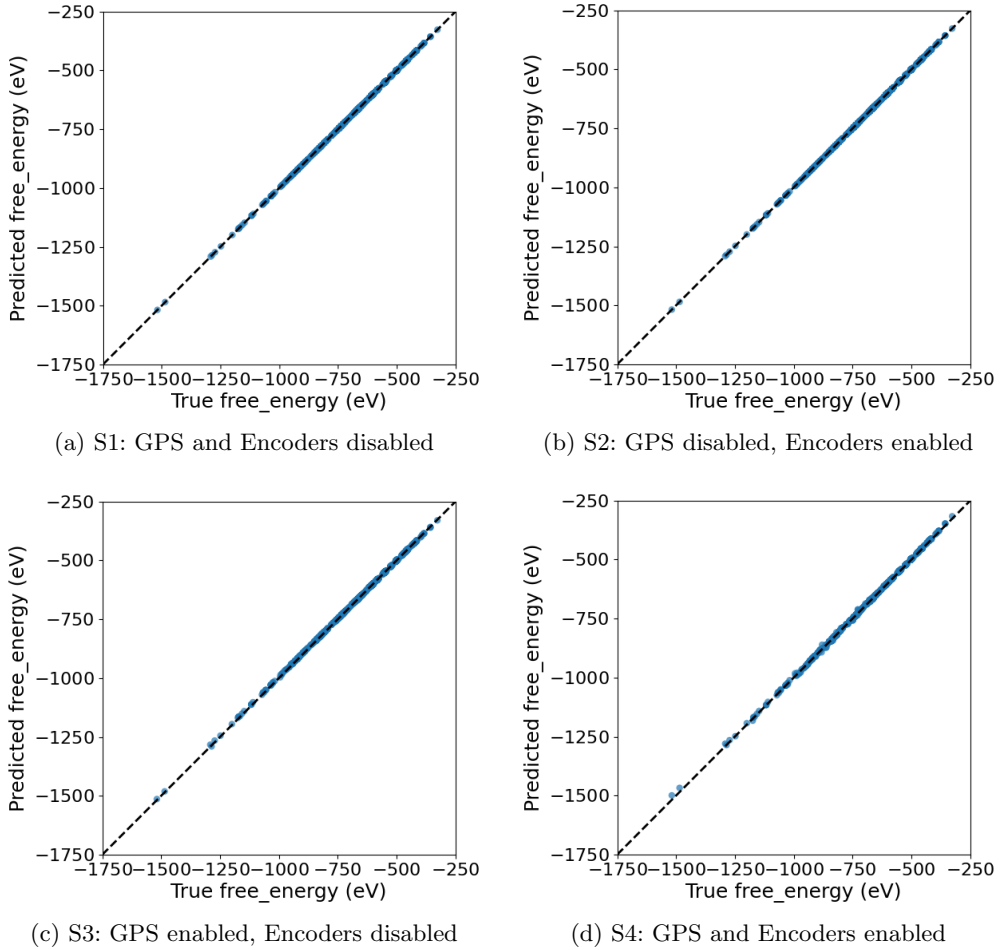


Fig. 5: QM9 parity plots (Predicted vs. True free energy) for the best HPO trial per scheme

Table 10: TMQM test performance per scheme

Scheme	MSE \downarrow	MAE \downarrow	Pearson $r\uparrow$
S1	0.000 008	0.002 009	0.999 169
S2	0.000004	0.001135	0.999598
S3	0.000 010	0.002 055	0.999 090
S4	0.000 006	0.001 843	0.999 560

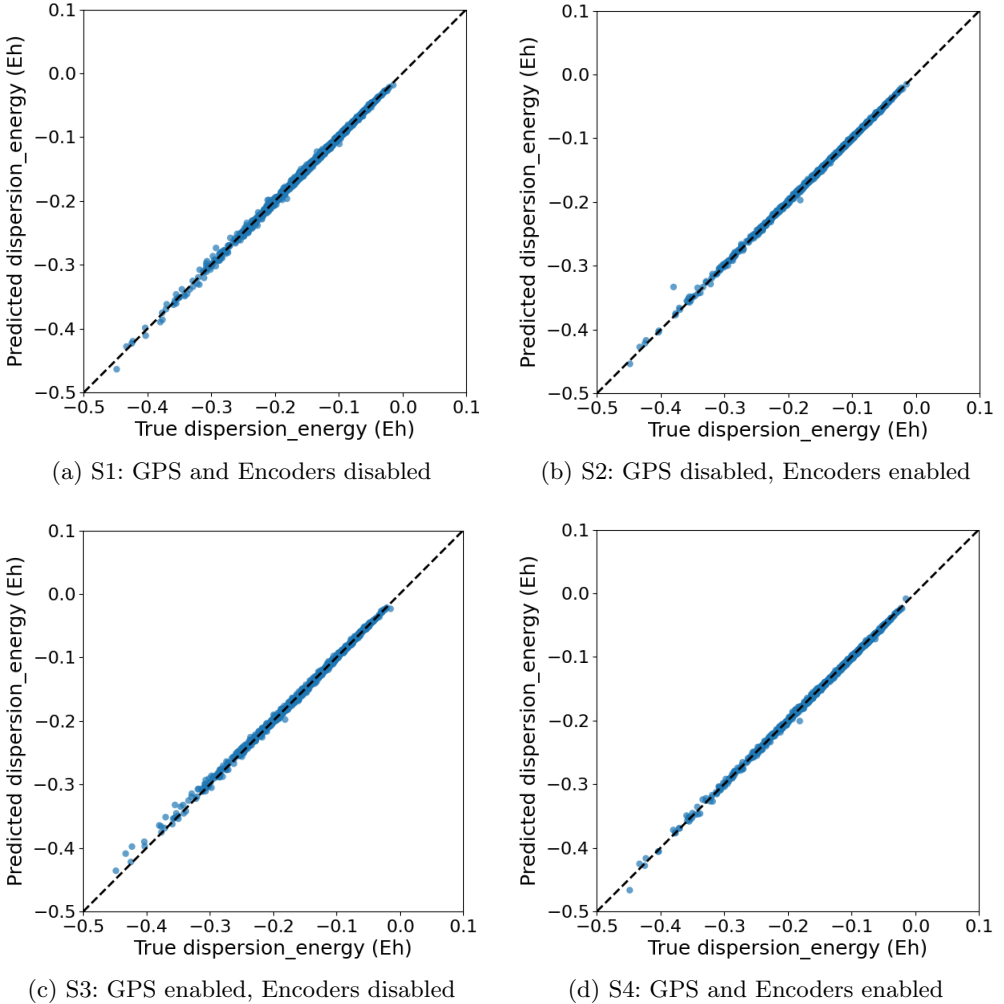


Fig. 6: TMQM parity plots (Predicted vs. True dispersion energy) for the best HPO trial per scheme.

4.4.4 NIAID

In this case, GPS provides modest but consistent improvements when paired with adequate width (Tables 11 and 12). **S4** achieves the best MSE and highest correlation, while **S2** (282.6k) attains the lowest MAE; both clearly outperform the smaller no-GPS baseline (**S1**, 98.3k). The gap between **S4** and **S2** is small (e.g., $\sim 1.8\%$ MSE), implying diminishing returns per parameter, yet the parity plots (Figure 7) show a slightly tighter envelope for **S4** across the full dynamic range, consistent with GPS aiding long-range charge redistribution effects. Deeper stacks are not required (3–4 conv layers suffice), but larger hidden/edge embeddings appear beneficial.

Table 11: NIAID best HPO configuration per scheme

Scheme	MPNN	#Conv	Hidden	EdgeEmb	GPS Heads	#Parameters
S1	PAINN	6	32	0	0	98 256
S2	PAINN	4	63	8	0	282 600
S3	PAINN	3	48	5	4	178 573
S4	PAINN	3	64	12	4	316 774

Table 12: NIAID test performance per scheme

Scheme	MSE \downarrow	MAE \downarrow	Pearson $r\uparrow$
S1	0.005 638	0.045 077	0.983 533
S2	0.004 462	0.039230	0.987 040
S3	0.005 426	0.045 755	0.984 630
S4	0.004381	0.039 690	0.987258

4.4.5 OGB-PCQM4Mv2

As shown in Table 14, the encoder-augmented PAINN without GPS (**S2**, 71.1k parameters) delivers the best MSE/MAE and highest r , while being smaller than the DimeNet baseline (**S1**, 95.1k) and much smaller than the GPS-heavy model (**S4**, 130.2k). Relative to **S1**, **S2** reduces MSE by $\sim 27\%$ with fewer parameters, and it outperforms **S4** by $\sim 18\%$ MSE despite a 45% smaller footprint, highlighting strong parameter efficiency. The parity plots are shown in Figure 8. **S2** shows the least widening of residuals in this regime, suggesting better calibration and smoothing of long-range interactions without the added complexity of GPS.

Table 13: OGB-PCQM4Mv2 best HPO configuration per scheme

Scheme	MPNN	#Conv	Hidden	EdgeEmb	GPS Heads	#Parameters
S1	DimeNet	5	38	0	0	95 051
S2	PAINN	2	45	9	0	71 084
S3	PAINN	3	32	13	2	82 280
S4	PAINN	3	40	10	8	130 203

4.4.6 OGB-PPA

Tables 15 and 16 show that the best accuracy is obtained by a moderately deep GPS model (**S4**, 3 conv, 2 heads) at 369.8k parameters, exceeding the strongest no-GPS baseline (**S1**, 86.2k) by 1.77 percentage points. However, the improvement comes at a $\sim 4\times$ parameter cost, and a deeper/wider no-GPS model (**S2**, 340.7k) underperforms

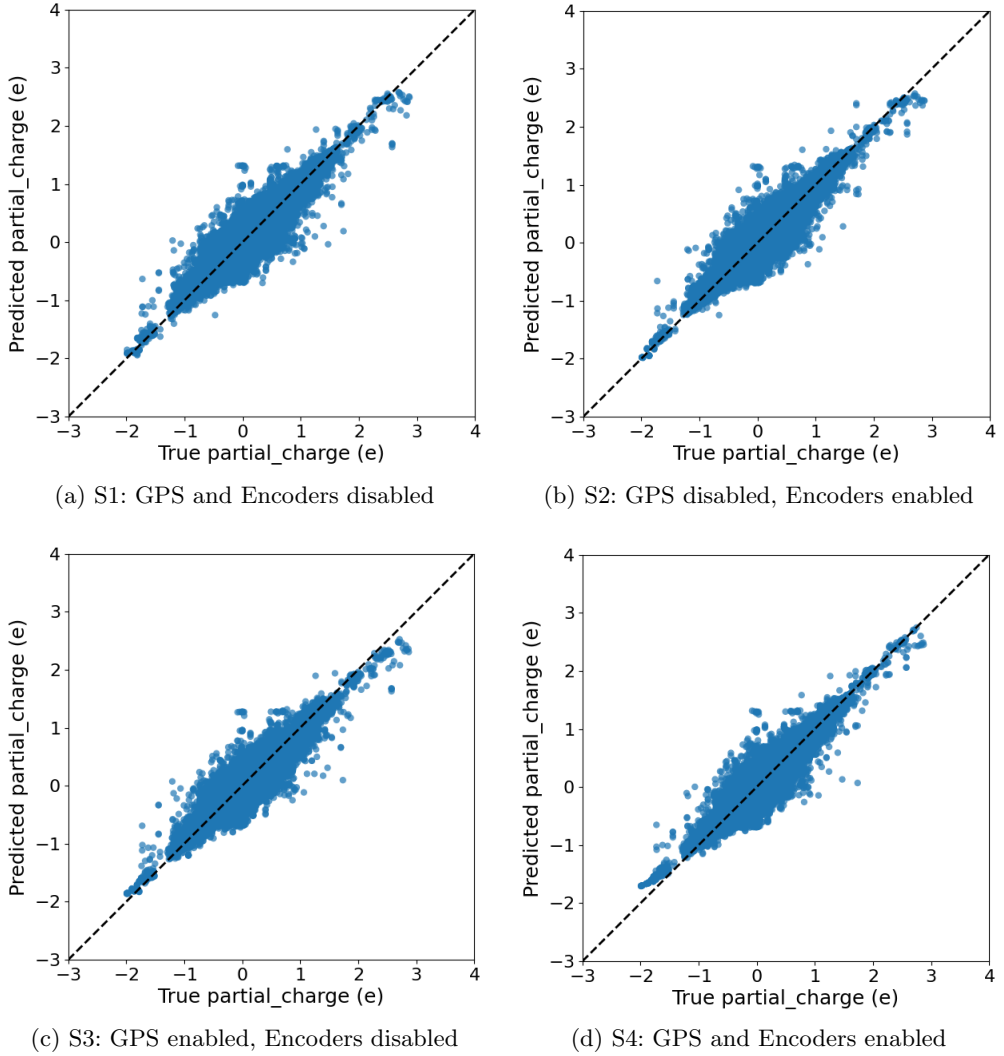


Fig. 7: NIAID parity plots (Predicted vs. True partial charge) for the best HPO trial per scheme

both **S1** and **S4**, indicating that capacity alone does not substitute for global information mixing. The shallow GPS model (**S3**, 65.1k) underachieves, suggesting that GPS is effective only when paired with sufficient hidden/edge capacity and moderate depth. Overall, PPA benefits from GPS, but the accuracy-per-parameter trade-off still favors compact baselines in settings where parameter budget is constrained.

Table 14: OGB-PCQM4Mv2 test performance per scheme

Scheme	MSE \downarrow	MAE \downarrow	Pearson $r\uparrow$
S1	0.041 413	0.141 160	0.984 880
S2	0.030317	0.124741	0.988888
S3	0.042 750	0.146 679	0.984 439
S4	0.037 168	0.135 053	0.986 146

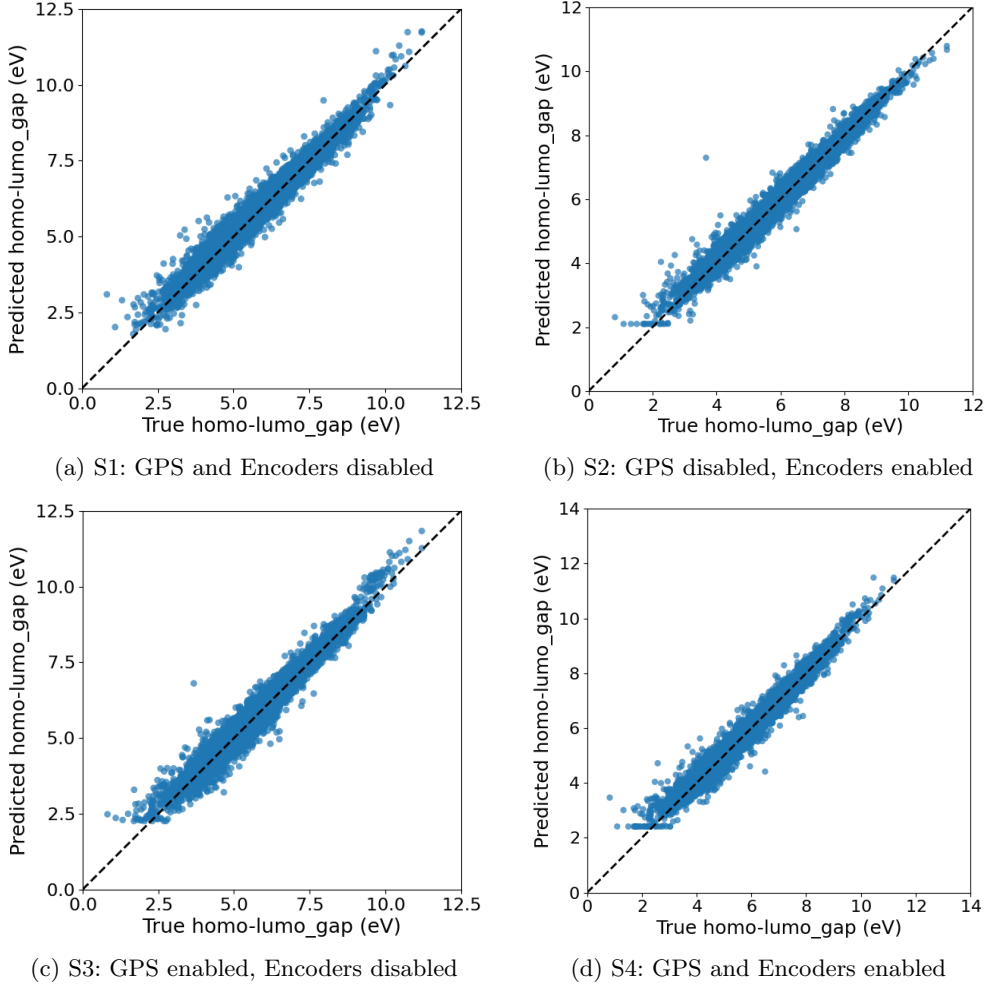


Fig. 8: OGB-PCQM4Mv2 parity plots (Predicted vs. True homolumo gap) for the best HPO trial per scheme

Table 15: OGB-PPA best HPO configuration per scheme

Scheme	MPNN	#Conv	Hidden	EdgeEmb	GPS Heads	#Parameters
S1	PNA	5	30	0	0	86 151
S2	PNA	5	56	19	0	340 728
S3	PNA	2	32	15	2	65 128
S4	PNA	3	64	22	2	369 804

Table 16: OGB-PPA test accuracy per scheme

	S1	S2	S3	S4
Accuracy (%) \uparrow	65.24	63.75	53.24	67.01

4.4.7 OGB-molPCBA

For molPCBA, GPS with PNA improves both accuracy and parameter efficiency (Table 17 and 18). The best configuration, **S3** (3 conv, 2 heads), reaches mAP = 0.184 with 215.8k parameters—outperforming the deeper no-GPS PNA (**S2**, 252.1k; +0.017 absolute, +10.2% relative) and the larger GAT baseline (**S1**, 304.3k; +0.029, +18.7%) while using fewer parameters. Increasing heads from 2 to 4 (**S4**, 217.0k) yields no additional gain, consistent with diminishing returns from global capacity once moderate long-range mixing is available. These results indicate that, for molPCBA, moderate depth with limited GPS is sufficient to exploit cross-task structure, and further scaling primarily inflates model size without commensurate improvements.

Table 17: OGB-molPCBA best HPO configuration per scheme

Scheme	MPNN	#Conv	Hidden	EdgeEmb	GPS Heads	#Parameters
S1	GAT	3	44	0	0	304 270
S2	PNA	5	48	8	0	252 106
S3	PNA	3	48	12	2	215 829
S4	PNA	3	48	12	4	216 969

Table 18: OGB-molPCBA test performance per scheme

	S1	S2	S3	S4
mAP \uparrow	0.155	0.167	0.184	0.182

5 Discussion

In contrast to prior work, our contribution is not to introduce yet another architecture, but to deliver the first unified framework for reproducible atomistic benchmarking that incorporates MPNNs, global attention, hybrid GPS-style models, and encoder-based feature augmentation under identical training, implementation, and hyperparameter optimization settings. This design enables us to isolate the effect of each modeling component—local message passing, global attention, and encoders—across diverse datasets, providing principled guidance on when attention mechanisms are truly beneficial. To our knowledge, no existing study has provided such a controlled evaluation.

Across datasets, our experiments clarify when encoder augmentations and global attention (GPS) provide measurable benefit, and at what computational cost. On small to mid-scale regression tasks (ZINC, QM9, TMQM), encoder-augmented PAINN without GPS is consistently competitive or best: on ZINC and QM9, the encoder-only setting (S2) yields the lowest errors while remaining compact (Tables 5–6, 7–8), and on TMQM a shallow PAINN with encodings (S2) again minimizes MSE/MAE despite being smaller than GPS variants (Tables 9–10). Parity plots (Figs. 4, 5, 6) show correlations near unity across schemes, with residual differences concentrated in a few high-magnitude outliers; in this regime, richer node/edge encodings deliver the dominant gains, and additional global information offers little benefit at similar budgets. In contrast, tasks with weaker local features or pronounced long-range dependence (OGB-PPA, OGB-PCBA) benefit moderately on use of GPS when paired with adequate width and edge capacity: on PPA, a moderately deep PNA+GPS model (S4; three convolutional layers, two GPS heads) improves top-1 accuracy over the strongest no-GPS baseline at higher parameter cost (Tables 15–16), while the shallower GPS model (S3) underperforms; on PCBA, PNA+GPS with two heads (S3) attains the highest mAP with fewer parameters than both the deeper no-GPS PNA (S2) and the larger GAT baseline (S1), and increasing heads to four (S4) yields diminishing returns (Tables 17–18). Collectively, these results indicate that moderate global information (two heads) and moderate depth (three message-passing layers) are sufficient to capture nonlocal effects in large, atomistic graphs, whereas encoder quality is the primary driver on chemically local regressions.

A second aspect is parameter efficiency. Across datasets, the best or near-best schemes typically fall in the tens to a few hundreds of thousands of parameters. For instance, on OGB-PCQM4Mv2, the encoder-augmented PAINN without GPS (S2; 71k parameters) achieves the lowest MSE/MAE and the highest correlation, outperforming both a deeper DimeNet baseline (S1; 95k) and a larger GPS model (S4; 130k) (Tables 13–14; Fig. 8). On PPA, the accuracy gain of S4 over S1 is modest relative to the $> 4 \times$ parameter increase; thus the baseline without GPS remains useful when the parameter budget is constrained. On NIAID, GPS yields small but consistent improvements in MSE and correlation (S4), whereas the lowest MAE is achieved without GPS (S2), underscoring that the best configuration can depend on the target metric (Tables 11–12; Fig. 7).

GraphGPS (Rampásek et al. 2022) popularized the hybrid recipe of local MPNN layers with GPS blocks and rich positional/structural encodings. The reference configurations reported for ZINC, PPA, PCBA, and PCQM4Mv2 are strong but operate at substantially higher capacity and depth than our study; for example, on PCQM4Mv2 the *gps-medium* setting employs 10 GPS layers with a hidden size in the mid–hundreds and a multi–million parameter budget (e.g., $\sim 9.5\text{M}$ parameters), and even “small” variants remain in the multi–million regime. These designs achieve excellent absolute scores but can be burdensome to reproduce exactly, owing to large memory footprints and sensitivity to hyperparameters and training infrastructure. Our experiments intentionally adopt small models with transparent toggles (encoders on/off; GPS on/off; heads and depth) and report parameter counts alongside metrics. This capacity-aware protocol exposes when GPS truly helps (PPA/PCBA) and when encoders alone suffice (ZINC/QM9/PCQM), and it facilitates fairer, more reproducible comparisons than matching against highly tuned, much larger systems.

For datasets with established SOTA baselines (ZINC, PCQM4v2, molPCBA etc.), we refrain from emphasizing raw numerical gaps to specific leader-boards and instead propose a *normalized, budget-controlled* evaluation: every result is paired with parameter counts and layer budgets (Tables above), and parity plots visualize the error structure beyond single-number summaries. For datasets without widely used SOTA leader-boards (TMQM, NIAID etc.), we provide compact, reproducible references together with parity plots, establishing a consistent yardstick for future work. Across tasks, three practical takeaways emerge: (i) encoder modules account for most of the gains on chemically local regressions; (ii) moderate GPS (two heads) improves classification on large, atomistic graphs when paired with adequate width and edge embeddings; and (iii) scaling GPS depth/heads beyond this point yields diminishing returns relative to parameter growth. Overall, exposing both architectural toggles and parameter counts offers a clearer and more reproducible basis for assessing progress than relying on large, in-replicable configurations.

6 Conclusions and Future Work

Conclusions. We presented a capacity–controlled, reproducible evaluation of local (MPNN), hybrid, and fused local–global graph architectures within a unified HydraGNN pipeline, isolating the effects of encoders and global attention (GPS) across regression and classification benchmarks. Three findings emerge. *First*, domain encoders are the dominant lever on chemically local regressions: on ZINC, QM9, TMQM, and PCQM, encoder-augmented PAINN without GPS consistently matches or exceeds alternatives while remaining compact, and parity plots indicate that remaining errors are concentrated in a few high-magnitude tails rather than systematic miscalibration. *Second*, GPS complements rather than replaces message passing: on OGB-PPA and OGB-PCBA, moderate global information mixing—two GPS heads paired with three message-passing layers and adequate hidden/edge capacity—yields the most reliable gains, whereas adding more heads or depth exhibits diminishing returns and under-sized GPS models underperform. *Third*, parameter efficiency matters: strong results are obtained with tens to a few hundreds of thousands of

parameters, often outperforming deeper baselines and approaching or surpassing much larger GPS variants; reporting metrics alongside parameter counts exposes the true accuracy–capacity trade-off and improves comparability. Practically, we recommend encoder-augmented MPNNs as the default, enabling GPS when targets depend on nonlocal context, and starting with small GPS budgets (two heads, three layers) before scaling width or heads. Beyond established leaderboards, we provide compact, transparent baselines and diagnostic plots for datasets lacking widely used references, offering a reproducible yardstick for future work and a clearer path to principled scaling under fixed compute budgets.

Future work. The present encoders omit explicit geometric features such as positional, distance and angular information; incorporating these is likely to improve geometry-sensitive tasks. Also, our current transformer model does not preserve equivariance which can be necessary for multiple physics-informed downstream tasks. Further, we did not study large-scale pretraining or sparse/linearized attention variants that could reduce the quadratic overhead. Extending the evaluation to larger bio-molecular and crystalline systems, adding uncertainty quantification, and exploring equivariant attention for vector/tensor targets are natural next steps. We expect the framework and results to serve as a reference point for method development and for principled decisions about when global attention is useful in atomistic graph learning.

6.1 Data Availability Statement

All datasets and all scripts used in this study are available on the GitHub repository: [HydraGNN](#)

7 Acknowledgement

This research is sponsored by the Artificial Intelligence Initiative as part of the Laboratory Directed Research and Development (LDRD) Program of Oak Ridge National Laboratory, managed by UT-Battelle, LLC, for the US Department of Energy under contract DE-AC05-00OR22725. This work used resources of the Oak Ridge Leadership Computing Facility, which is supported by the Office of Science of the U.S. Department of Energy under Contract No. DE-AC05-00OR22725, under ASCR Leadership Computing Challenge (ALCC) award LRN070.

References

- (2020) Ogb: Graph property prediction datasets. Open Graph Benchmark documentation, URL <https://ogb.stanford.edu/docs/graphprop/>
- (2022) Pcq4mv2. Open Graph Benchmark (OGB-LSC) documentation, URL <https://ogb.stanford.edu/docs/lsc/pcqm4mv2/>

Alon U, Yahav E (2021a) On the bottleneck of graph neural networks and its practical implications. In: International Conference on Learning Representations, URL <https://openreview.net/forum?id=i80OPhOCVH2>, arXiv:2006.05205

Alon U, Yahav E (2021b) On the bottleneck of graph neural networks and its practical implications. In: International Conference on Learning Representations (ICLR), URL <https://arxiv.org/abs/2006.05205>

Baker J, Lupo-Pasini M, Hauck C (2023) Invariant features for accurate predictions of quantum chemical uv-vis spectra of organic molecules. ChemRxiv (working paper), <https://doi.org/10.26434/chemrxiv-2023-9n306>

Balaprakash P, Salim M, Uram TD, et al (2018) Deephyper: Asynchronous hyperparameter search for deep neural networks. In: 25th International Conference on High Performance Computing (HiPC), IEEE, pp 42–51

Balcells D, Skjelstad BB (2020) tmqm dataset—quantum geometries and properties of 86k transition metal complexes. Journal of Chemical Information and Modeling 60(12):6135–6146. <https://doi.org/10.1021/acs.jcim.0c01041>, URL <https://doi.org/10.1021/acs.jcim.0c01041>

Bartlett RJ, Musial M (2007) Coupled-cluster theory in quantum chemistry. Reviews of Modern Physics 79(1):291–352. <https://doi.org/10.1103/RevModPhys.79.291>

Battaglia PW, Hamrick JB, Bapst V, et al (2018) Relational inductive biases, deep learning, and graph networks. arXiv preprint arXiv:180601261

Batzner S, Musaelian A, Sun L, et al (2022) E(3)-equivariant graph neural networks for data-efficient and accurate interatomic potentials. arXiv preprint arXiv:210103164

Behler J, Parrinello M (2007) Generalized neural-network representation of high-dimensional potential-energy surfaces. Physical Review Letters 98(14):146401. <https://doi.org/10.1103/PhysRevLett.98.146401>

Benson SW (1976) Thermochemical Kinetics: Methods for the Estimation of Thermochemical Data and Rate Parameters, 2nd edn. Wiley, New York

Born M, Mayer JE (1932) Zur gittertheorie der ionenkristalle. Zeitschrift für Physik 75:1–18. <https://doi.org/10.1007/BF01340511>

Bronstein MM, Bruna J, Cohen T, et al (2021) Geometric deep learning: Grids, groups, graphs, geodesics, and gauges. URL <https://arxiv.org/abs/2104.13478>, arXiv:2104.13478

Burner J, Luo J, White A, et al (2022a) ab initio repeat charge mof database (arc-mof). Zenodo, <https://doi.org/10.5281/zenodo.6908727>, URL <https://zenodo.org/records/6908728>

Burner J, Luo J, White A, et al (2022b) Arc–mof: A diverse database of metal–organic frameworks with dft-derived partial atomic charges and descriptors for machine learning. ChemRxiv, <https://doi.org/10.26434/chemrxiv-2022-mvr06>, URL <https://chemrxiv.org/engage/chemrxiv/article-details/62e04636cf661270d7b615c1>

Burner J, Luo J, White A, et al (2025) ab initio repeat charge mof database (arc-mof). Dataset on Zenodo, <https://doi.org/10.5281/zenodo.6908727>, URL <https://zenodo.org/record/6908727>

Butler KT, Davies DW, Cartwright H, et al (2018) Machine learning for molecular and materials science. *Nature* 559(7715):547–555. <https://doi.org/10.1038/s41586-018-0337-2>

Casimir HBG, Polder D (1948a) The influence of retardation on the london–van der waals forces. *Physical Review* 73:360–372. <https://doi.org/10.1103/PhysRev.73.360>

Casimir HBG, Polder D (1948b) The influence of retardation on the london–van der waals forces. *Physical Review* 73(4):360–372. <https://doi.org/10.1103/PhysRev.73.360>

Cherkasov A, Muratov EN, Fourches D, et al (2014) Qsar modeling: Where have you been? where are you going? *Journal of Medicinal Chemistry* 57(12):4977–5010. <https://doi.org/10.1021/jm4004285>

Choi JY, Zhang P, Mehta K, et al (2022) Scalable training of graph convolutional neural networks for fast and accurate predictions of homo-lumo gap in molecules. arXiv preprint arXiv:220711333 <https://doi.org/10.48550/arXiv.2207.11333>, arXiv:2207.11333 [cs.LG]

Duvenaud DK, Maclaurin D, Aguilera-Iparraguirre J, et al (2015) Convolutional networks on graphs for learning molecular fingerprints. In: Advances in Neural Information Processing Systems, URL <https://papers.nips.cc/paper/2015/hash/f9be311e65d81a9ad8150a60844bb94c-Abstract.html>

Dwivedi VP, Bresson X (2020) A generalization of transformer networks to graphs. In: AAAI Workshop on Graph Representation Learning

Dwivedi VP, Rampášek L, Galkin M, et al (2022) Long range graph benchmark. In: Advances in Neural Information Processing Systems (NeurIPS), Datasets and Benchmarks Track, <https://doi.org/10.48550/arXiv.2206.08164>, URL <https://arxiv.org/abs/2206.08164>

Egelé R, Guyon I, Vishwanath V, et al (2023) Asynchronous decentralized Bayesian optimization for large scale hyperparameter optimization. In: IEEE 19th International Conference on e-Science (e-Science), IEEE, pp 1–10, <https://doi.org/10.1109/e-Science58273.2023.10254839>

Frenkel D, Smit B (2002) Understanding Molecular Simulation: From Algorithms to Applications, 2nd edn. Academic Press, San Diego

Fuchs FB, Worrall DE, Fischer V, et al (2020) Se(3)-transformers: 3d roto-translation equivariant attention networks. In: NeurIPS, URL <https://proceedings.neurips.cc/paper/2020/file/15231a7ce4ba789d13b722cc5c955834-Paper.pdf>

Garcia Satorras V, Hoogeboom E, Welling M (2021) E(n) equivariant graph neural networks. In: Proceedings of the 38th International Conference on Machine Learning, Proceedings of Machine Learning Research, vol 139. PMLR, pp 9323–9332, URL <https://proceedings.mlr.press/v139/satorras21a.html>, arXiv:2102.09844

Gilmer J, Schoenholz SS, Riley PF, et al (2017) Neural message passing for quantum chemistry. In: Proceedings of the 34th International Conference on Machine Learning (ICML), Proceedings of Machine Learning Research, vol 70. PMLR, pp 1263–1272

Gregoire JM, Xiang C, Liu X, et al (2013) High-throughput experimentation and screening for materials design. Annual Review of Materials Research 43:63–81. <https://doi.org/10.1146/annurev-matsci-070813-113234>

Grimme S, Antony J, Ehrlich S, et al (2010) A consistent and accurate *ab initio* parametrization of density functional dispersion correction (dft-d) for the 94 elements h–pu. The Journal of Chemical Physics 132(15):154104. <https://doi.org/10.1063/1.3382344>

Hamilton W, Ying Z, Leskovec J (2017) Inductive representation learning on large graphs. In: Advances in Neural Information Processing Systems (NeurIPS), arXiv:1706.02216

Hammett LP (1937) The effect of structure upon the reactions of organic compounds. benzene derivatives. Journal of the American Chemical Society 59(1):96–103

Hu W, Fey M, Ren H, et al (2020a) Open graph benchmark: Datasets for machine learning on graphs. In: Proceedings of the 34th International Conference on Neural Information Processing Systems, Curran Associates Inc., pp 1–17

Hu W, Fey M, et al (2020b) Open graph benchmark: Datasets for machine learning on graphs. arXiv preprint arXiv:200500687 URL <https://arxiv.org/abs/2005.00687>

Hu W, et al (2021) Ogb-lsc: A large-scale challenge for machine learning on graphs. arXiv preprint arXiv:210309430 URL <https://arxiv.org/abs/2103.09430>

Irwin JJ, Shoichet BK (2005a) Zinc—a free database of commercially available compounds for virtual screening. Journal of chemical information and modeling 45(1):177–182. <https://doi.org/10.1021/ci049714+>

Irwin JJ, Shoichet BK (2005b) Zinc—a free database of commercially available compounds for virtual screening. *Journal of Chemical Information and Modeling* 45(1):177–182. <https://doi.org/10.1021/ci049714+>

Israelachvili JN (2011) *Intermolecular and Surface Forces*, 3rd edn. Academic Press, San Diego

Jeziorski B, Moszyński R, Szalewicz K (1994) Perturbation theory approach to intermolecular potential energy surfaces of van der waals complexes. *Chemical Reviews* 94(7):1887–1930. <https://doi.org/10.1021/cr00031a008>

Kearnes S, McCloskey K, Berndl M, et al (2016) Molecular graph convolutions: moving beyond fingerprints. *Journal of Computer-Aided Molecular Design* 30(8):595–608. <https://doi.org/10.1007/s10822-016-9938-8>

Kipf TN, Welling M (2017) Semi-supervised classification with graph convolutional networks. In: International Conference on Learning Representations (ICLR), [arXiv:1609.02907](https://arxiv.org/abs/1609.02907)

Klicpera J, Giri S, Margraf J, et al (2020a) Dimenet++: Faster and stronger directional message passing. arXiv preprint [arXiv:2011.14115](https://arxiv.org/abs/2011.14115)

Klicpera J, Groß J, Günnemann S (2020b) Directional message passing for molecular graphs. In: International Conference on Learning Representations, URL https://iclr.cc/virtual_2020/poster_B1eWbxStPH.html

Klicpera J, Groß J, Günnemann S (2020c) Directional message passing for molecular graphs. In: International Conference on Learning Representations (ICLR)

Klicpera J, Groß J, Günnemann S (2020d) Directional message passing for molecular graphs. International Conference on Learning Representations (ICLR)

Kohn W, Sham LJ (1965) Self-consistent equations including exchange and correlation effects. *Physical Review* 140(4A):A1133–A1138. <https://doi.org/10.1103/PhysRev.140.A1133>

Kreuzer D, Beaini D, Létourneau V, et al (2021) Rethinking graph transformers with spectral attention. In: Advances in Neural Information Processing Systems

Li Q, Han Z, Wu X (2018a) Deeper insights into graph convolutional networks for semi-supervised learning. AAAI Conference on Artificial Intelligence (workshop/extended version: arXiv:1801.07606) URL <https://arxiv.org/abs/1801.07606>, [arXiv:1801.07606](https://arxiv.org/abs/1801.07606)

Li Q, Han Z, Wu XM (2018b) Deeper insights into graph convolutional networks for semi-supervised learning. In: Proceedings of the Thirty-Second AAAI Conference on Artificial Intelligence (AAAI), pp 3538–3545, URL <https://arxiv.org/abs/1801.07606>

Liao Y, Wood BM, Das A, et al (2024) Equiformer2: Improved equivariant transformer for scaling to higher-degree representations. In: International Conference on Learning Representations (ICLR), URL <https://openreview.net/forum?id=mCOBKZmrzD>, arXiv:2306.12059

London F (1937a) The general theory of molecular forces. *Transactions of the Faraday Society* 33:8–26. <https://doi.org/10.1039/TF937330008B>

London F (1937b) The general theory of molecular forces. *Transactions of the Faraday Society* 33:8b–26. <https://doi.org/10.1039/TF937330008B>

Lupo-Pasini M, Burcul M, Reeve ST, et al (2022a) Fast and accurate predictions of total energy for solid solution alloys with graph convolutional neural networks. In: Nichols J, Maccabe AB, Nutaro J, et al (eds) *Driving Scientific and Engineering Discoveries Through the Integration of Experiment, Big Data, and Modeling and Simulation (SMC 2021)*, Communications in Computer and Information Science, vol 1512. Springer, Cham, p 79–98, https://doi.org/10.1007/978-3-030-96498-6_5

Lupo-Pasini M, Zhang P, Reeve ST, et al (2022b) Multi-task graph neural networks for simultaneous prediction of global and atomic properties in ferromagnetic systems. *Machine Learning: Science and Technology* 3(2):025007. <https://doi.org/10.1088/2632-2153/ac6a51>, arXiv:2202.01954

Lupo-Pasini M, Jung GS, Irle S (2023) Graph neural networks predict energetic and mechanical properties for models of solid solution metal alloy phases. *Computational Materials Science* 224:112141. <https://doi.org/10.1016/j.commatsci.2023.112141>

Lupo-Pasini M, Choi JY, Mehta K, et al (2025a) Scalable training of trustworthy and energy-efficient predictive graph foundation models for atomistic materials modeling: a case study with hydragnn. *The Journal of Supercomputing* 81:618. <https://doi.org/10.1007/s11227-025-07029-9>

Lupo-Pasini M, Zhang P, Choi JY, et al (2025b) Transferable predictions of energetic and structural properties for refractory solid solution alloys across chemical compositions. *Computational Materials Science* 257:113908. <https://doi.org/10.1016/j.commatsci.2025.113908>

Mardirossian N, Head-Gordon M (2017) Thirty years of density functional theory in computational chemistry: an overview and extensive assessment of 200 density functionals. *WIREs Computational Molecular Science* 7(1):e1319. <https://doi.org/10.1002/wcms.1319>

Masters D, Dean J, Klaser K, et al (2023a) Gps++: Reviving the art of message passing for molecular property prediction. arXiv preprint arXiv:230202947 <https://doi.org/10.48550/arXiv.2302.02947>, URL <https://arxiv.org/abs/2302.02947>

Masters D, Dean J, Klaser K, et al (2023b) Gps++: Reviving the art of message passing for molecular property prediction. arXiv preprint arXiv:230202947

Maziarka L, Danel T, Mucha S, et al (2020) Molecule attention transformer. arXiv preprint arXiv:200208264 URL <https://arxiv.org/abs/2002.08264>

Nakata M, Shimazaki T (2017) Pubchemqc project: A large-scale first-principles electronic structure database for data-driven chemistry. *Journal of Chemical Information and Modeling* 57(6):1300–1308. <https://doi.org/10.1021/acs.jcim.7b00083>

Oono K, Suzuki T (2020a) Graph neural networks exponentially lose expressive power for node classification. In: International Conference on Learning Representations, URL <https://openreview.net/forum?id=S1ldO2EfPH>, arXiv:1905.10947

Oono K, Suzuki T (2020b) Graph neural networks exponentially lose expressive power for node classification. In: International Conference on Learning Representations (ICLR), URL <https://arxiv.org/abs/1905.10947>

Parr RG, Yang W (1989) Density-Functional Theory of Atoms and Molecules. Oxford University Press, New York

Plaxco KW, Simons KT, Baker D (1998) Contact order, transition state placement and the refolding rates of single domain proteins. *Journal of Molecular Biology* 277(4):985–994. <https://doi.org/10.1006/jmbi.1998.1645>

Ramakrishnan R, Dral PO, Rupp M, et al (2014a) Quantum chemistry structures and properties of 134 kilo molecules. *Scientific data* 1(1):140022. <https://doi.org/10.1038/sdata.2014.22>

Ramakrishnan R, Dral PO, Rupp M, et al (2014b) Quantum chemistry structures and properties of 134 kilo molecules. *Scientific Data* 1:140022. <https://doi.org/10.1038/sdata.2014.22>, URL <https://www.nature.com/articles/sdata201422>

Rampášek L, Galkin M, Dwivedi VP, et al (2022) Recipe for a general, powerful, scalable graph transformer. *Advances in Neural Information Processing Systems* arXiv:2205.12454 [cs.LG]

Rampášek L, Galkin M, Dwivedi VP, et al (2022) Recipe for a general, powerful, scalable graph transformer. In: Advances in Neural Information Processing Systems (NeurIPS), URL https://proceedings.neurips.cc/paper_files/paper/2022/hash/5d4834a159f1547b267a05a4e2b7cf5e-Abstract-Conference.html, arXiv:2205.12454

Ruddigkeit L, van Deursen R, Blum LC, et al (2012a) Enumeration of 166 billion organic small molecules in the chemical universe database gdb-17. *Journal of chemical information and modeling* 52(11):2864–2875. <https://doi.org/10.1021/ci300415d>

Ruddigkeit L, van Deursen R, Blum LC, et al (2012b) Enumeration of 166 billion organic small molecules in the chemical universe database gdb-17. *Journal of Chemical Information and Modeling* 52(11):2864–2875. <https://doi.org/10.1021/ci300415d>

Rupp M, Tkatchenko A, Müller KR, et al (2012) Fast and accurate modeling of molecular atomization energies with machine learning. *Physical Review Letters* 108(5):058301. <https://doi.org/10.1103/PhysRevLett.108.058301>

Satorras VG, Hoogeboom E, Welling M (2021) E(n) equivariant graph neural networks. *Proceedings of the 38th International Conference on Machine Learning (ICML)* <https://doi.org/10.48550/arXiv.2102.09844>, pMLR; arXiv:2102.09844

Schütt KT, Kindermans PJ, Saucedo HE, et al (2018a) Schnet: A continuous-filter convolutional neural network for modeling quantum interactions. *Journal of Chemical Theory and Computation* 14(8):4161–4170

Schütt KT, Saucedo HE, Kindermans P, et al (2018b) Schnet – a deep learning architecture for molecules and materials. *The Journal of Chemical Physics* 148(24):241722. <https://doi.org/10.1063/1.5019779>

Schütt KT, Unke OT, Gastegger M (2021) Equivariant message passing for the prediction of tensorial properties. In: *International Conference on Machine Learning (ICML)*

Smith JS, Isayev O, Roitberg AE (2017) Ani-1: an extensible neural network potential with dft accuracy at force field computational cost. *Chemical Science* 8(4):3192–3203. <https://doi.org/10.1039/C6SC05720A>

Sterling T, Irwin JJ (2015) Zinc15—ligand discovery for everyone. *Journal of Chemical Information and Modeling* 55(11):2324–2337. <https://doi.org/10.1021/acs.jcim.5b00559>

Stone AJ (2013) *The Theory of Intermolecular Forces*, 2nd edn. Oxford University Press, Oxford

Szklarczyk D, et al (2019) String v11: Protein–protein association networks with increased coverage, supporting functional discovery in genome-wide experimental datasets. *Nucleic Acids Research* 47(D1):D607–D613. <https://doi.org/10.1093/nar/gky1131>

Taft RW (1952) Polar and steric substituent constants for aliphatic and *o*-benzoate groups from rates of esterification and hydrolysis of esters. *Journal of the American Chemical Society* 74(12):3120–3128

Thomas N, Smidt T, Kearnes S, et al (2018) Tensor field networks: Rotation- and translation-equivariant neural networks for 3d point clouds. arXiv preprint

arXiv:1802.08219 URL <https://arxiv.org/abs/1802.08219>

Tönshoff J, Ritzert M, Rosenbluth E, et al (2023) Where did the gap go? reassessing the long-range graph benchmark. arXiv preprint arXiv:230900367

Topping J, Di Giovanni F, Nikolentzos G, et al (2022) Understanding over-squashing and bottlenecks on graphs via curvature. In: International Conference on Learning Representations, URL <https://openreview.net/forum?id=Vb-8mjZrj1>, arXiv:2111.14522

Trinajstić N (1992) Chemical Graph Theory, 2nd edn. CRC Press, Boca Raton, classic reference for graph distances on molecular bond graphs

Vaswani A, Shazeer N, Parmar N, et al (2017) Attention is all you need. In: Advances in Neural Information Processing Systems

Veličković P, Cucurull G, Casanova A, et al (2018) Graph attention networks. In: International Conference on Learning Representations (ICLR), arXiv:1710.10903

Ward L, Agrawal A, Choudhary A, et al (2016) A general-purpose machine learning framework for predicting properties of inorganic materials. npj Computational Materials 2:16028. <https://doi.org/10.1038/npjcompumats.2016.28>

Wu Z, Ramsundar B, Feinberg EN, et al (2018) Moleculenet: A benchmark for molecular machine learning. Chemical Science 9:513–530. <https://doi.org/10.1039/C7SC02664A>

Wu Z, Pan S, Chen F, et al (2021) A comprehensive survey on graph neural networks. IEEE Transactions on Neural Networks and Learning Systems 32(1):4–24. <https://doi.org/10.1109/TNNLS.2020.2978386>

Xu K, Hu W, Leskovec J, et al (2019) How powerful are graph neural networks? In: International Conference on Learning Representations (ICLR), arXiv:1810.00826

Ying C, Cai T, Luo S, et al (2021a) Do transformers really perform badly for graph representation? In: Advances in Neural Information Processing Systems

Ying C, Cai T, Luo S, et al (2021b) Do transformers really perform badly for graph representation? In: Advances in Neural Information Processing Systems (NeurIPS), URL <https://proceedings.neurips.cc/paper/2021/hash/f1c1592588411002af340cbaedd6fc33-Abstract.html>, graphormer, arXiv:2106.05234

Ying C, Cai T, Luo S, et al (2021c) Do transformers really perform badly for graph representation? In: NeurIPS, URL <https://proceedings.neurips.cc/paper/2021/file/f1c1592588411002af340cbaedd6fc33-Paper.pdf>

Zaheer M, Kottur S, Ravanbakhsh S, et al (2017) Deep sets. In: Advances in Neural Information Processing Systems, URL <https://proceedings.neurips.cc/paper/2017/>

hash/f22e4747da1aa27e363d86d40ff442fe-Abstract.html, arXiv:1703.06114

Zhou G, Gao Z, Ding Q, et al (2023a) Uni-mol: A universal 3d molecular representation learning framework. In: The Eleventh International Conference on Learning Representations, URL <https://openreview.net/forum?id=6K2RM6wVqKu>

Zhou G, Gao Z, Ding Q, et al (2023b) Uni-mol: A universal 3d molecular representation learning framework. In: International Conference on Learning Representations (ICLR), URL <https://openreview.net/forum?id=6K2RM6wVqKu>

Zhou J, Cui G, Zhang Z, et al (2020) Graph neural networks: A review of methods and applications. AI Open 1:57–81. <https://doi.org/10.1016/j.aiopen.2021.01.001>